COMBUSTION CHARACTERISTICS OF ADDITIVELY MANUFACTURED GUN PROPELLANTS

by

Aaron Afriat

A Thesis

Submitted to the Faculty of Purdue University

In Partial Fulfillment of the Requirements for the degree of

Master of Science in Mechanical Engineering

School of Mechanical Engineering

West Lafayette, Indiana

May 2021

THE PURDUE UNIVERSITY GRADUATE SCHOOL
STATEMENT OF COMMITTEE APPROVAL

Dr. Steven F. Son, Chair
School of Mechanical Engineering

Dr. Jay P. Gore, Member
School of Mechanical Engineering

Dr. Terrence R. Meyer, Member
School of Mechanical Engineering

Approved by:
Dr. Nicole L. Key

The entirety of this work is dedicated to my mother Raquel, my father Jacques and my grandmother Madeleine, for their relentless support and words of wisdom throughout my degree.

ACKNOWLEDGMENTS

First of all, I would like to express my most profound gratitude towards my advisor, mentor and friend, Dr. Steven Son. His immense dedication to his students' success as well as his timeliness, openness and fairness are some of the many qualities I admire him for. My co-workers and friends at Purdue University played a major role in my professional success and my personal well-being. Notably, I would like to thank Julio Hernandez, Joey Yount, Julie Bach and Monique McClain. Finally, I owe thanks to my sisters Liora and Anna for their moral support and for being a unique source of motivation.

The work in this thesis was funded by the Strategic Environmental Research and Development Program (SERDP) Grant No. W912HQ19C0063. This exceptional program gave me the privilege to synthesize, formulate, 3D print and extensively test innovative gun and rocket propellants, many of which I had never done before. Additional thanks are due to Dr. Jeffrey Rhoads, Timothy Manship, Trevor Fleck, John McCaw and Stephanie Andress for their collaboration throughout this work which far exceeded expectations.

TABLE OF CONTENTS

LIST OF TABLES

LIST OF FIGURES

ABSTRACT

Additive manufacturing of gun propellants is an emerging and promising field which addresses the limitations of conventional manufacturing techniques. Gun propellants are manufactured using wetted extrusion, which uses volatile solvents and dies of limited and constant geometries. On the other hand, additive techniques are faced with the challenges of maintaining the gun propellant's energetic content as well as its structural integrity during high pressure combustion. The work presented in this thesis demonstrates the feasibility of producing functioning gun propellant grains using vibration-assisted 3D printing, a novel method which has been shown to extrude extremely viscous materials such as clays and propellant pastes. At first, the technique is compared to screw-driven additive methods which have been used in printing gun propellant pastes with slightly lower energetic content. In chapter two, diethylene glycol dinitrate (DEGDN), a highly energetic plasticizer, was investigated due to its potential to replace nitroglycerin in double base propellants with high nitroglycerin content. A novel isoconversional method was applied to analyze its decomposition kinetics. The ignition and lifetime values of diethylene glycol dinitrate were obtained using the new isoconversional method, in order to assess the safety of using the plasticizer in a modified double base propellant. In chapter three, a modified double base propellant (M8D) containing DEGDN was additively manufactured using VAP. The printed strands had little to no porosity, and their density was nearly equal to the theoretical maximum density of the mixture. The strands were burned at high pressures in a Crawford bomb and the burning was visualized using high speed cameras. The burning rate equation as a function of the M8D propellant as a function of pressure was obtained. Overall, this work shows that VAP is capable of printing highly energetic gun propellants with low solvent content, low porosity, with high printing speeds, and which have consistent burning characteristics at high pressures.

1. COMPARING THE CAPABILITIES OF VIBRATION-ASSISTED PRINTING (VAP) AND DIRECT-WRITE ADDITIVE MANUFACTURING TECHNIQUES

1.1 Introduction

Additive manufacturing (AM) is a manufacturing method that has received considerable attention in recent years. This broad category encompasses many different methods of building up a part using layer-by-layer addition. Efforts have been made to leverage the advantages of AM in printing composite slurries for applications such as magnets, ceramics, and propellants. In most of these applications, the quality of the final part improves as the solids loading of the slurry increases, but high solids loadings also correspond to high viscosity, which tends to be a limiting factor in the additive manufacturing of slurries. Stereolithography reaches its maximum solids loading at about 40% by volume, and the popular fused-filament fabrication (FFF) method runs into difficulty when producing workable filament from these materials. In this context, direct write (DW) will be defined as the continuous extrusion of an ink onto the substrate or previous layer using back pressure. DW has been used by several groups to print highly-loaded composite slurries. Shen et al. printed magnets from 45μm NdFeB powder in a polymer binder using DW [1]. In a later study, they explored bimodal slurries of plate-like particles at solids loadings of up to 65vol% [2]. Both studies used a photo-curing polymer binder. Additionally, Chen et al. evaluated the use of DW with ceramics, concluding that DW is an effective method for printing freestanding structures because the high particle content minimizes shrinkage, cracks, and sagging [3]. Similarly, it is clear from Muravyev's review of additively manufactured propellants that DW is currently the method of choice for highly loaded energetics of millimeter scale or greater [4]. As demonstrated by Chandru et al., this method of printing offers intriguing possibilities for printing propellants, particularly with novel geometries [5]. Geometric freedom is an AM advantage of particular interest in manufacturing propellant. Grain geometry strongly impacts burning characteristics through burning surface area, and AM offers the possibility of optimizing geometry through novel shapes impossible using traditional manufacturing methods such as casting and extrusion [6]. DW has proven capable and versatile, although the method lacks a certain finesse in flow control. Li et al. addressed this issue by comparing a standard syringe/plunger DW method to a needle valve

and to an auger valve [7]. In addition, viscosity continues to be an issue. The highest solids loadings achieved have used very fine particles (<50μm) and nozzle diameters on the order of 1 mm, negatively impacting feature resolution. No study reviewed could print using greater than 70% solids by volume.

A new DW method called "vibration-assisted printing" (VAP) was recently developed by Gunduz et al. [8]. They were able to print high viscosity inks ($\mu > 10{,}000$ Pa·s) from a nozzle diameter of 600 μm using high-amplitude ultrasonic vibrations induced at the nozzle tip and a back-pressure of 690 kPa. The flow rate at this pressure without ultrasonic vibrations was 0.59 mm/s, but this rate increased to 107 mm/s when the ultrasonic vibrations were induced. This system was used by McClain et al. to print ammonium perchlorate (AP) composite propellants at solids loadings up to 76vol% [9]. Two polymer binder mixtures were used, hydroxyl-terminated polybutadiene (HTPB) and a UV-curing polyurethane. The resulting samples were evaluated for their quality as propellant with particular regard to porosity, and they compared favorably with traditionally cast propellants. In this study, the new VAP method was compared to the standard syringe/plunger DW method. The purpose of this study was to explore questions of print shape fidelity, print speed, and overall print quality with specific emphasis on the use of each to print highly viscous materials.

1.2 Methods

1.2.1 Experimental Setup

Two different printers were used in this project. First, a new vibration-assisted (VAP) printer was designed, building upon the original design developed at Purdue University [8]. Viscous ink was stored in high-density polypropylene syringes with an exit diameter measured at 0.5 mm. Ultrasonic vibrations at 28.2 kHz were applied to the tip of the syringe. The vibrations were generated using a function generator and an amplifier connected to a transformer. To enable continuous flow, a moderate back-pressure was applied to the syringe reservoir using a commercial air compressor (0.5 to 0.65 MPa). Prior to printing, the print head was primed until the flow rate and print temperature were nearly constant to minimize inconsistencies between prints.

The baseline printer, an established commercial 3D printer (Hyrel 3D Engine SR) with a direct write head (Hyrel 3D KR2 15), was used to represent commercial direct ink write (DW) printing options. A motor-driven power screw provided back pressure to the material. The stainless-steel syringe included a fitting such that a 2.54 cm long disposable probe needle (Grainger) could be attached. A test, discussed later, was conducted to evaluate the minimum needle inner diameter printable using the Sculpey™ clay ink. For all of the subsequent tests, a probe needle with an inner diameter of 838 μm was used.

Sculpey™ polymer clay was chosen to be the ink. No thinning compound or materials were added that could change the composition of the clay. This material was used because it is an inert material and was considered to be an inexpensive substitute for highly viscous composite materials. After printing, each print was cured at 130 °C for 15 min per 6.8 mm of material.

1.2.2 Specimen

Shapes were chosen to demonstrate the respective qualities of each printer. First, a zigzag line containing a range of angles from 10° to 100° in 10° increments was printed on each printer. Each line was printed at the highest head travel speed where the printer could maintain a steady printed line without obvious shearing or defects. The turning capabilities of the printers were demonstrated. Additional shapes were printed to demonstrate overall shape quality and to push each system to the limits of its capabilities with regards to speed and precision. These shapes were chosen from benchmarking elements designed for FFF 3D printing [10]. Next, two shapes were printed to demonstrate the capability of each system to print overhanging faces. On one overhang shape, the angled faces were fully detached from adjoining faces, while on the other the angled faces were connected. In the first, the overhang angles ranged from 20° to 70° in 5° increments, while in the connected overhang print the overhang angles ranged from 0° to 30° in 5° increments. Finally, several shapes were printed to evaluate the quality of negative features inside solid objects. These shapes included solid cylinders with one or more vertical cylindrical holes and solid cylinders with a cone-shaped internal void to evaluate minimum printable hole diameters. In addition, cylinders with no solid perimeters and various infill densities were printed to explore free-standing structures of less than full density. The cylinders were printed with 50% infill in the central core and 70% in

the outer perimeter. Effort was made to optimize slicing parameters and print settings for each printer system. The prints shown in this paper were printed with the best settings attained. Two commercial slicing software programs, Slic3r and Simplify3D, were used to generate print paths and parameters based on the STL file.

1.2.3 Viscometry

The viscosity of clay was measured at room temperature using a digital viscometer (Brookfield DVE). A T-bar spindle (Brookfield T-F) was driven at various rpm values through a 4 oz cylindrical container filled with clay. The spindle was specifically designed for high viscosity materials and soft-solids whose viscosity cannot be measured using standard spindles. Although shear rate cannot be computed from the rotation of a T-bar spindle, the viscosity data provides a useful measure of the soft solid's structural strength. During each trial, viscosity values were recorded as a function of position in the cylinder and an average value was computed. At 2, 6 and 10 rpm, the average viscosity measured 299.5, 112.4 and 78.2 MPa•s, respectively. These values suggest that clay is in the shear-thinning regime. The viscosity of clay is higher than a typical propellant slurry whose viscosity reaches upwards of 1.5 MPa at a solids loading of 80 vol.%, a fact that suggests that clay can be used as a challenging surrogate ink for highly-loaded slurries [11].

1.2.4 Nozzle Diameter

Nozzle diameter on extrusion-based AM printers is a significant parameter that influences print quality. To achieve fine detail resolution, a small nozzle is desired. When printing the viscous clay, nozzle diameters smaller than 0.8 mm proved to be too mechanically demanding for the commercial DW printer considered here. Tests were conducted to assess which diameter should be used. Using a consistent extrusion multiplier setting, a printed line was attempted using the following nozzle diameters: 1.524 mm, 1.194 mm, 0.838 mm, 0.584 mm, 0.483 mm, 0.406 mm, and 0.356 mm. A nozzle diameter of 0.838 mm was chosen for subsequent tests. Although print quality was a factor in this evaluation, the principal standard was finding the smallest nozzle diameter which did not cause the print head motor gears to skip. As further evidence that this study pushed the print head to its maximum, over the course of the study, the brass power screw fitting

was completely stripped and had to be replaced. In contrast, VAP can easily print with a 0.5 mm nozzle diameter. However, due to the limited variety and compatibility of polypropylene syringes on the market, nozzle diameters smaller than 0.5 mm were not explored in this study.

1.2.5 Analysis

A variety of imaging and analysis techniques were utilized to evaluate the quality of each print. Still images of each completed print were recorded using a Sony α7R III camera equipped with a FE2.8/90 macro lens as well as a fluorescent lighting, daylight, (FLD) filter. Three-dimensional scans of each print were taken using a Shining3D EinScan-SP optical scanner. GOM Inspect, a commercial 3D inspection software, was used to evaluate the quality of printed shapes relative to the designed shapes. A high resolution 3D X-ray Microtomography scanner (Skyscan 1272) was used to inspect the internal geometries of the cylinders with graded gyroidal infills. Avizo 2019 was used to 3D-render the reconstructed images and calculate the porosity through the length of the sample. The density was then compared to the density calculated using a variation of Archimedes' method. A lump of cured clay was weighed and its volume was computed from 3D optical scans. The density of clay was calculated from the mass and volume. 3D optical scans of the cylindrical samples were used to find their volume, and their density was calculated based on the density of cured clay. To inspect internal geometries, inverted cones and perforated cylinders were sectioned using a low-speed precision saw (Buehler) equipped with an electroplated diamond wafering blade. To minimize fracture due to the brittleness of the clay, these samples were filled with transparent epoxy resin (EpoFix) at a mixing ratio of 25:3 by weight, and left to cure for 12 hr. The samples were then polished to prevent damage to the sample during processing.

1.3 Results

1.3.1 Turning Angle

To compare the turning ability of the two printers, zig-zag lines with turning angles ranging from 10° to 100° were printed (Figure 1.1). Each sample was printed at the highest speed possible while ensuring minimal to no surface defect of the clay. The DW sample exhibits significant angled bulges at the tip of each corner, increasing in severity as the turning angle becomes sharper. In

contrast, the VAP sample shows sharper corners with less deformation at the turn radius. This result is notable given that the VAP sample was printed at 5000 mm/min, 50x greater than the DW's 100 mm/min. Higher printing speeds were tested for the DW printer, but were unsuccessful.

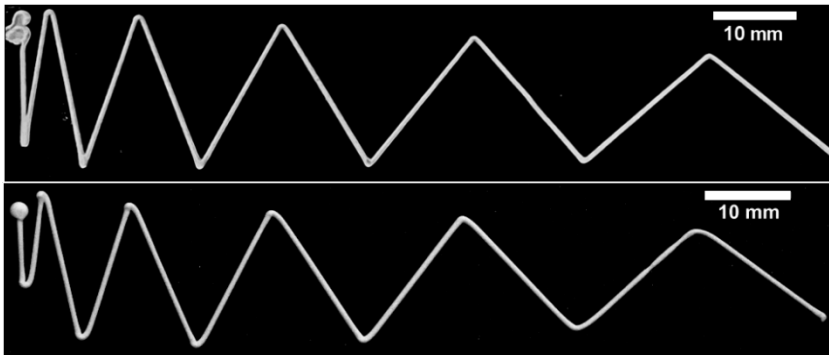

Figure 1.1. Printed zig zag samples. Top: VAP sample. Bottom: DIW sample.

To ensure that the line of ink did not shear or break, the extrusion rate had to be increased, as well as the print head velocity, but the print head extrusion motor was straining and skipping, even at the extrusion rate necessary for smooth printing at 100 mm/min. Faster rates were considered likely to damage the print head.

One major disadvantage of extrusion-based AM techniques is their relative lack of resolution in sharp turns. In addition, turning angle is an important factor when printing complex geometries with constant turns, such as gyroidal and honeycomb geometries. The mathematical error length, defined as the length between the outermost corner of the paste and the intersection of the lines defined by the zigzag, is modeled by Equation 1 [12],

$$Error = \frac{r}{sin\left(\frac{\theta}{2}\right)} - r \tag{1}$$

Where r is the radius of the maximum circumscribed circle and θ is the designed turning angle. In practice, this error does not take into account the typical tool path computed by the slicing software (Figure 1.2). This error length was computed using ImageJ, and a plot of the normalized error (error/nozzle radius) to the turning angle was generated. The normalized error allows comparison between both printing techniques, taking into account the respective nozzle diameter used by each printing method. The error length can then be compared to the mathematical model, as defined by Equation 1.

Although both the VAP and DW techniques are extrusion-based methods, there is a clear discrepancy in their turning angle performance when printing clay (Figure 1.3). The VAP seems to approach the mathematical model more closely than the DW. As the turning angle is reduced, the difference in normalized error between the two methods is accentuated. For instance, at a 10° turning angle, the normalized error rises up to 20.8 for the DW, while the VAP's increases a couple of points from the previous turning angle measuring 20°. The discrepancy could stem from a variety of causes, including built-in velocity and extrusion controls. Print speed may also be a factor, although its contribution has not been quantified.

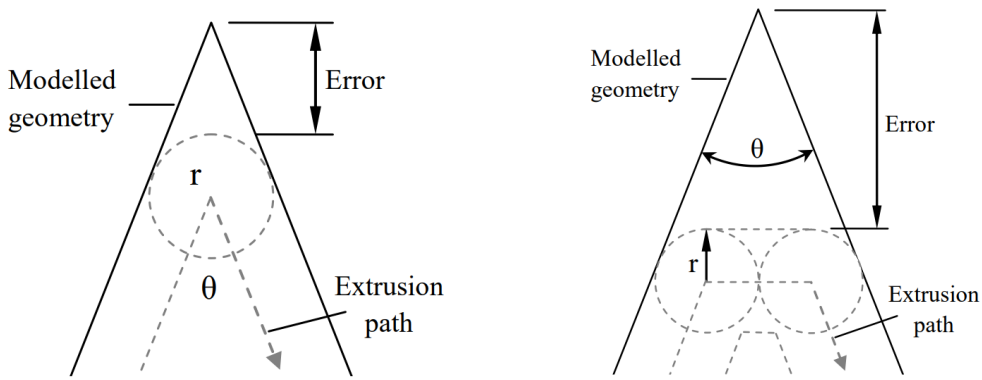

Figure 1.2. Left: error path from nozzle circularity. Right: actual error length due to tool path generation software. [12]

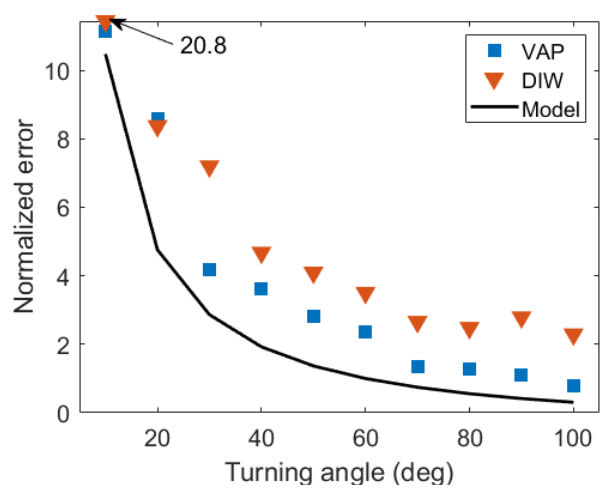

Figure 1.3. Normalized error computed against designed turn angle values. The error was normalized with respect to the radius of the nozzle used by VAP and DW methods. A curve of the mathematical model was included for comparison.

1.3.2 External Shape Analysis

Benchmarking Samples

Next, this study evaluated the quality of the 3D-printed shapes' external surfaces. A variety of shapes were selected from FFF benchmarking designs to evaluate both printers with respect to overhang angles, flat and curved surfaces, fine details, and overall quality. Three shapes were printed: a 3D Benchy, a supported-overhang shape, and a shape with positive and negative spherical elements (Figure 1.4). The 3D Benchy was printed at 50% scale relative to the open source design [13] because of the limited amount of ink storage in the printer syringe. This illustrates one of the shortcomings of many direct-write-based printing systems, which use a reservoir as opposed to filament. In addition, the 3D Benchy demonstrated several other quality aspects of each printer. First, the VAP printer, with its smaller-diameter ink nozzle, was able to print finer feature resolution than was the DW printer. In particular, the VAP print included such details as the twin holes in the top front of the hull as well as a small, vertical post on the deck. Also, in spite of the VAP's faster extrusion rate and print head velocity, the VAP was able to produce a cleaner print overall. Unlike the DW print, the VAP Benchy did not suffer from irregular and bulging lines of ink around sharp corners. However, the one notable area where the DW printer surpassed the VAP was in the cabin roof. While neither printer could produce a fully-formed roof structure, the DW printer was able to complete a few unbroken strands bridging the door frame gap, whereas the VAP printer could not bridge the gap at all. When trying to bridge gaps such as this, the VAP ink tended to sag and break. As observed previously by Gunduz et al., the ultrasonic vibrations applied to the nozzle reduce friction in part through the formation of shear planes and partial liquefaction [8]. Although Gunduz observed a near-instantaneous return to normal pressure-induced flow rates when the vibrations were removed, it is possible that the clay exited the nozzle in a partially liquefied state, resulting in the sagging observed here.

The supported overhang and hemispherical shapes likewise provided a comparison in shape and surface quality. For both, the printed shapes were scanned in 3D and compared to the original STL model using GOM Inspect software (Figure 1.5). The average deviation from best fit values for the supported overhang shape were 0.10 mm for the VAP and 0.18 mm for the DW. For the hemispherical shape, the values were 0.08 mm and 0.14 mm respectively. The surface degree-of-

deviation comparisons show the differences were primarily due to surface quality, rather than the structure's overall shape. While neither printer produced fully smooth surfaces or sharp corners, comparison shows that the finer ink extrusion diameter of the VAP produced better overall surface quality, as well as a sharper corner angle.

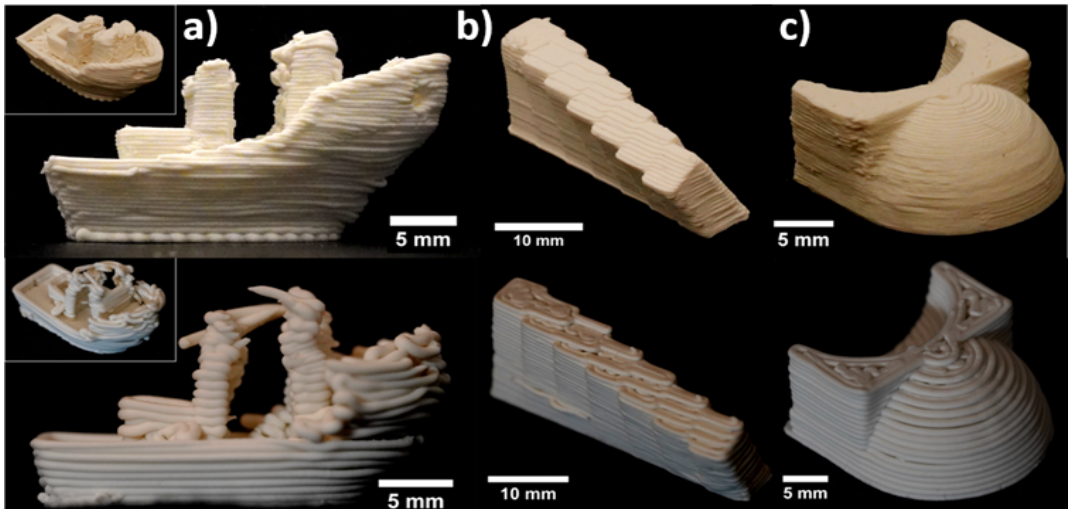

Figure 1.4. Sample of shapes printed for visual comparison. VAP samples are shown on top and DIW samples are shown below. a) 3D Benchy [13], b) supported overhang model, and c) positive/negative hemisphere shape.

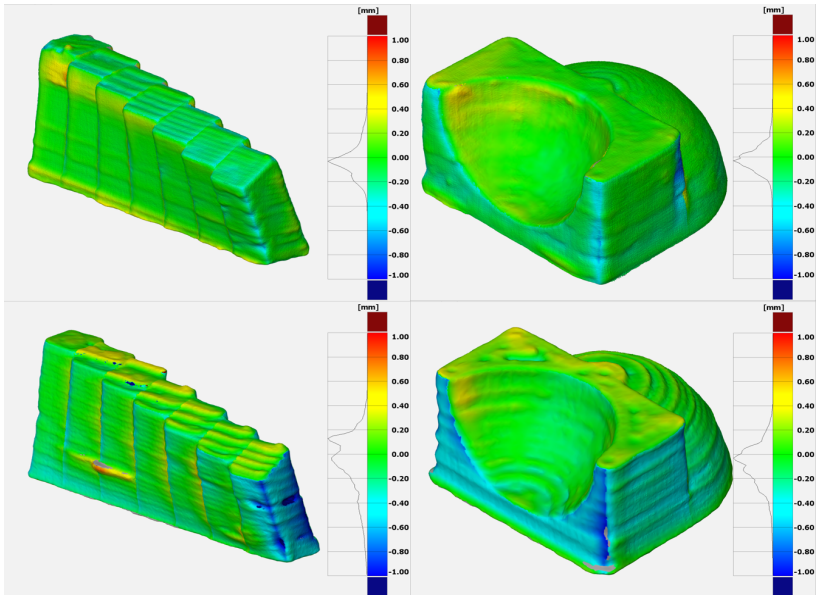

Figure 1.5. GOM Inspect surface comparison between STL and as-printed shapes. VAP prints are shown on top and DW prints are shown on the bottom. Colors range from 1 mm out from designed surface (red) to 1 mm inside designed surface (blue). A histogram shows the frequency of different surface deviations. VAP print settings: 5000 mm/min, 0.3 mm layer height, rectilinear infill, 0.60 MPa for a print time of 12 min . DW settings: 100 mm/min, 0.6 mm layer height, rectilinear infill, print time 40 min.

Cones

Three sets of cones with aspect ratios of 2.25, 3.0, and 4.25 were printed to allow a mathematical shape comparison (Figure 1.6). To evaluate the shapes, the cones were treated like two-dimensional triangles. A MATLAB code was prepared to identify points along the two angled sides and evaluate the resulting lines for straightness. The R-squared value for each side of the cone were averaged. It should be mentioned that the line analysis did not take into account the depth of photos of the cones, which may introduce additional error. The R-squared value of the small, medium and large cones were 0.989, 0.979 and 0.996, for the VAP samples, and 0.988, 0.982, and 0.985 for the DW samples, respectively. Taking the average and standard deviation of these values showed that, while the VAP samples have straighter, smoother edges, the DW samples were more consistent. Both sets of samples were very similar in quality, based on this metric. Some inconsistent layers, bulges, and dents visible on the VAP cones resulted from motor inaccuracies, and sometimes from a sudden increase in flow rate.

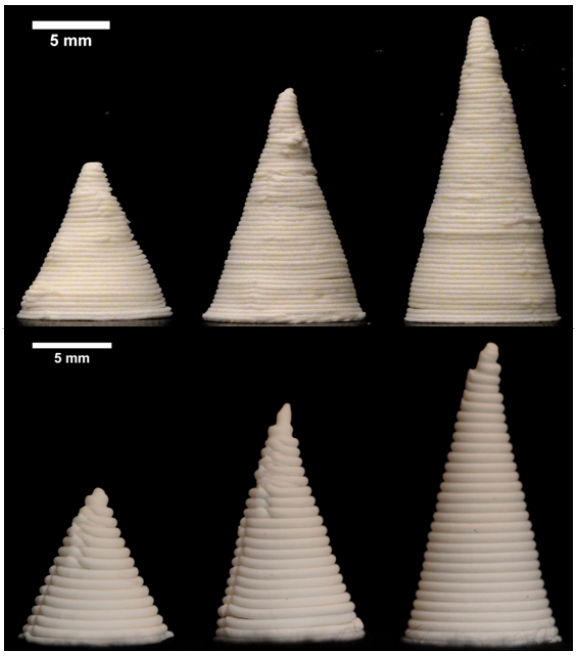

Figure 1.6. Cones with aspect ratios of 2.25, 3.0 and 4.25. VAP settings: 5500 mm/min, 0.3 mm layer height, 0.62 MPa for a print time of 4 min. DW settings: 100 mm/min, 0.6 mm layer height, print times 7, 11, and 14 min. respectively.

Overhang

A shape was designed to test the two printers' ability to produce overhanging surfaces. The shape includes 11 unsupported faces with overhang angles ranging from 20° to 70° in 5° increments (Figure 1.7). Once printed and cured, each angled face was photographed and the overhang angle measured using ImageJ. For the VAP sample, the as-printed angle is consistently less than the designed angle. The angle difference is principally attributed to sagging during the first few layers. As the layers increased, the forward sagging increased, which eventually caused a print failure. In addition, the VAP sample exhibited more sagging as the overhang angle increased. The printing of this shape was attempted 35 times on the VAP, with the 70° face printing successfully once. Only faces with angles smaller than 60 degrees printed consistently. The sagging appeared to be caused by the partial liquefaction of the clay due to the ultrasonic vibrations [14], which may have momentarily decreased the clay's viscosity. In contrast, the DW printer showed a surprising ability to print high overhang angles without significant sagging, even though larger layer heights were used. However, at extreme angles, subsequent layers were disconnected from each other to produce an irregular angled surface. Even at the high overhang angles, though, the print finished successfully.

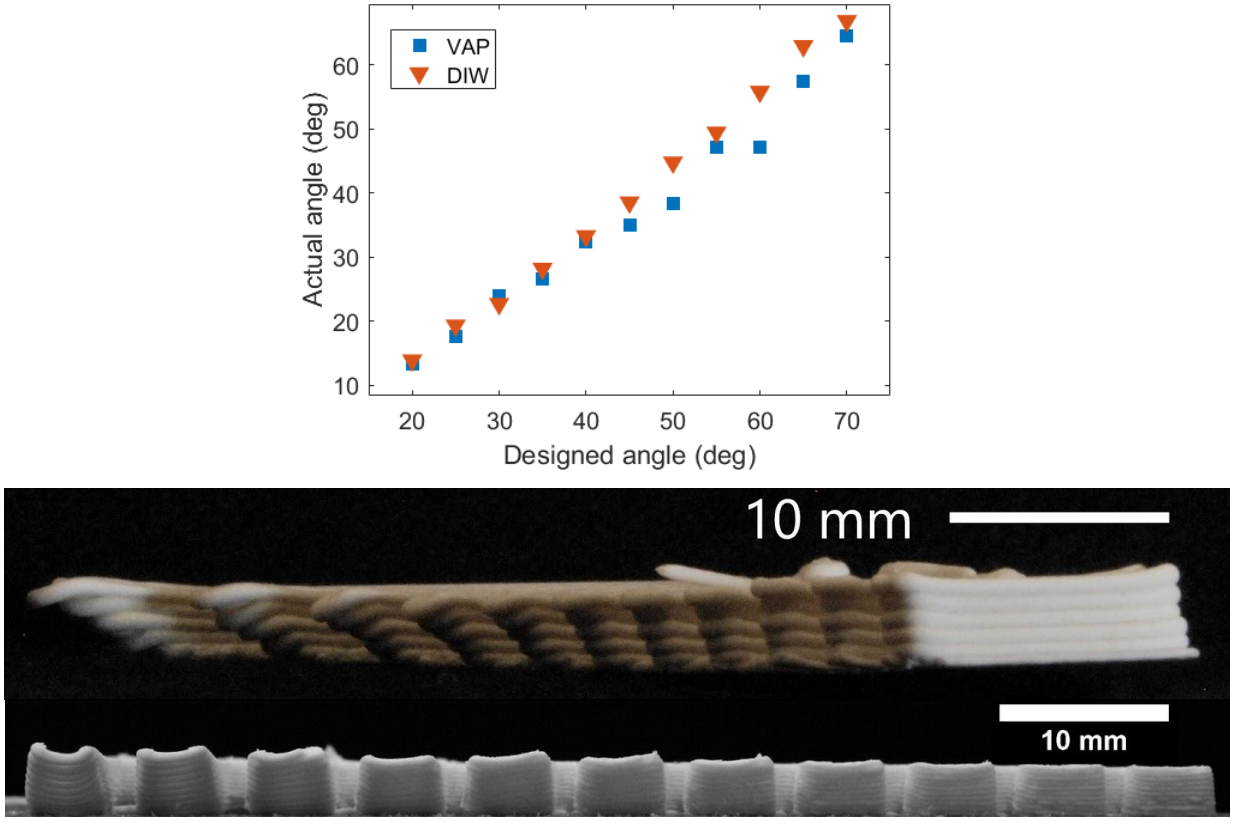

Figure 1.7. Top: overhang angles compared to designed values with R_{VAP}=0.993 and R_{DW}=0.960. Middle: Angled front view of Hyrel sample with disconnected layers visible. Bottom: Front view of sample printed with VAP with sagging visible at higher overhang angles. Masking tape was used as the print surface. VAP print settings: 180 0mm/min, 0.15 mm layer height, no infill, 0.52 MPa for a print time of 9 min. DW settings: 100 mm/min, 0.6 mm layer height, no infill, print time 2 hr.

1.3.3 Internal Shape Analysis

Negative Cones

An additional series of shapes were printed to evaluate the shape quality of negative features inside objects. First, solid cylinders were printed with a cone of empty space in the middle (Figure 1.8). The shapes were cured, filled with clear epoxy, and then cut in perpendicular cross-section, revealing the empty half-cone interior. The cut face was photographed using a high-contrast lens to aid discrimination between adjacent regions of highlight and shadow and to enable accurate visual measurements. The smallest-diameter circular hole discernible in each was measured using ImageJ software. The authors defined the minimal hole diameter as the diameter of the hole formed by the first layer of the inverted cone, and this value was 0.13 mm for the VAP sample and 0.34

mm for the DW sample. While this measurement was intended to give an idea of the smallest diameter hole each printer could resolve, the method used included considerable error. First, only one aspect ratio of the negative cone was printed due to time constraints. A steeper cone angle may have resulted in a smaller first layer hole diameter. In addition, error may have resulted from not slicing the shape in half at precisely the center of the negative cone. In spite of the error, however, visual inspection of the samples clearly shows that the thin VAP layers produce a cleaner, more sharply-defined cone point than do the thicker layers of the DW shape.

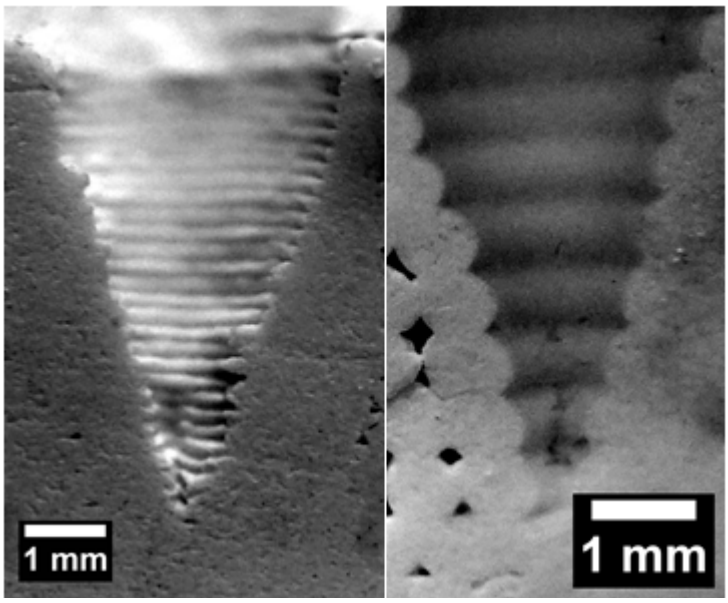

Figure 1.8. Internal cross section of an inverted cone. The cones were printed at a 16° half angle. Left: VAP. Right: DIW. A gap can be seen between the outermost layer and the infill on the DIW sample, but this did not affect the inner diameters.

Single Perforation Cylinders

The same process was used to evaluate the hole of a single-perforation cylinder (Figure 1.9). While the designed hole diameter was 3 mm, the average inner diameter of the VAP sample measured 2.04 mm with a standard deviation of 0.14 mm. On the DW sample, the average inner diameter measured 2.70 mm with a standard deviation of 0.14 mm. The discrepancy between the designed and actual inner diameter was mostly due to how an STL file is sliced for printing. The print path follows the designed geometry, and the syringe tip's movements are centered on the print path. When the extrudate diameter is non-negligible, the deviations from the designed geometry are likewise non-negligible. Since this overlap is a factor in most extrusion-driven additive

manufacturing methods, it will need to be accounted for when designing parts where the need for geometric accuracy is significant. It should be noted here that the internal voids seen in the DW sample are due to the low infill percentage used. However, infill percentage did not impact surface geometry or quality to any noticeable degree.

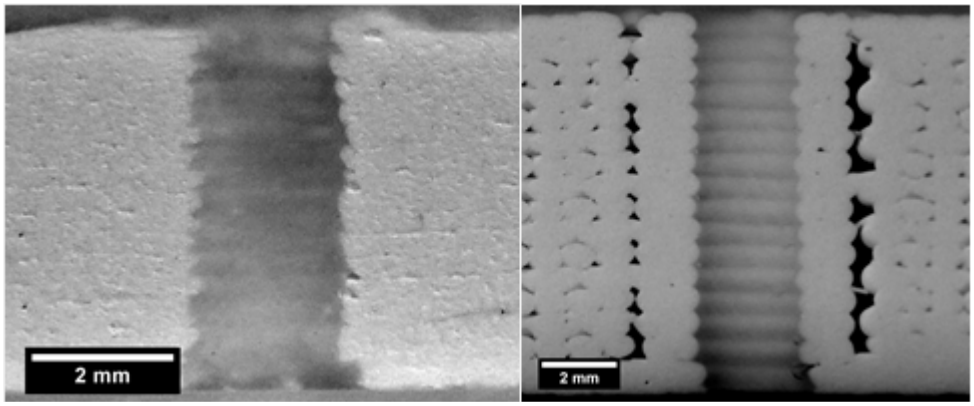

Figure 1.9. Internal cross section of a perforated cylinder. Left: VAP. Right: DIW. A gap can be seen between the outermost layer and the infill on the DIW sample, but this did not affect the inner diameters.

Multi-perforated Cylinders

Finally, cylinders containing an array of 19 perforations were attempted on each printer to explore their capabilities in creating small negative features and producing them in an array (Figure 1.10). The dimensions of the cylinder and array were taken from large-caliber gun propellant. Only the VAP was able to print the cylinder as-designed with hole diameters around 0.2 mm. Even so, the small perforations were imperfectly defined, with extraneous clay obscuring the holes on certain layers. The DW printer could not print the cylinder as-designed, owing primarily to the inability of the large-diameter nozzle of the DW printer to navigate the narrow spaces between the outer row of perforations and the wall of the cylinder. Even at 1.5 scale, the DW printer had difficulty filling in the space between perforations. Only at 2.0 scale could a reasonable approximation of the perforated cylinder be printed by the DW printer.

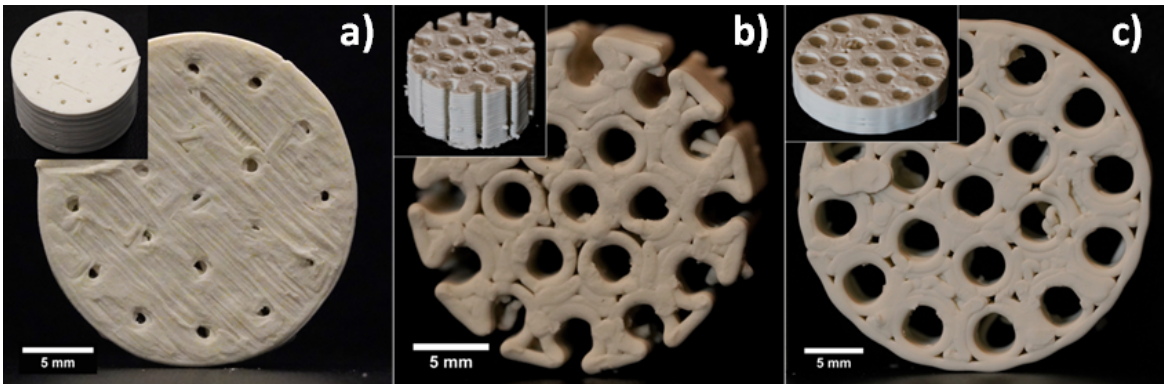

Figure 1.10. 19-performation arrays. a) VAP sample, b) DW sample at 1.5 scale, c) DW sample at 2.0 scale. VAP settings: 5000 mm/min, 0.3 mm layer height, rectilinear infill, 0.55 MPa for a print time of 12 min. DW settings: 100 mm/min, 0.6 mm layer height, rectilinear infill, print time 1 hr and 1.25 hr respectively.

1.3.4 Porosity Analysis: Loose Infill and Internal Porosity

Using highly loaded composite slurries to print lattices of less than full density and that are self-supporting even when uncured would be of interest in multiple applications. In addition, changing the burning surface area of a solid propellant grain is a principal mechanism for changing its performance, and manipulating infill parameters offers unique ways of accomplishing this. To explore these possibilities, a cylinder with graded infill was printed using the gyroidal infill pattern from the Slic3r software. The outer cylinder was at 70% infill while the inner cylinder was at 50% infill. To evaluate the porosity, and thus the internal surface area, of each, the samples were scanned using a MicroCT scanner. The scans were conducted using a resolution of 1632x1092 and an image pixel size of 15.8 μm. A filter of 0.5 Al + 0.038 Cu was used with a 0.4° rotation step. The reconstructed 3D images were rendered in Avizo 2019 and filtered using an iterative median filter with 26 neighborhood operations and 5 iterations (Figure 1.11). A binary 3D image was created using an interactive thresholding function. The porosity of the image as a function of height was then calculated using a ratio of voxels at each height (Figure 1.12). The average porosity was computed and compared to the value found using Archimedes' method. The percent differences of the porosities between Archimedes' method and Avizo were calculated to be 3.4% for the VAP sample and 5.4% for the DW sample. Greater variation in porosity per height was observed in the DW sample. This appeared to result partially from the larger nozzle diameter used and partially from sample defects on the top surface.

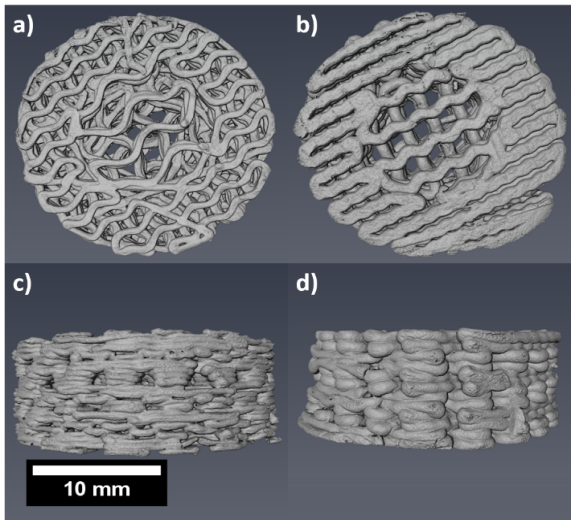

Figure 1.11. Rendering of the reconstructed MicroCT scan images. a) VAP top view, b) DW top view, c) VAP side view, d) DW side view. VAP print settings: 5000 mm/min, 0.3 mm layer height, 0.60 MPa for a print time of 7 min. DW settings: 100 mm/min, 0.6 mm layer height, print time 40 min.

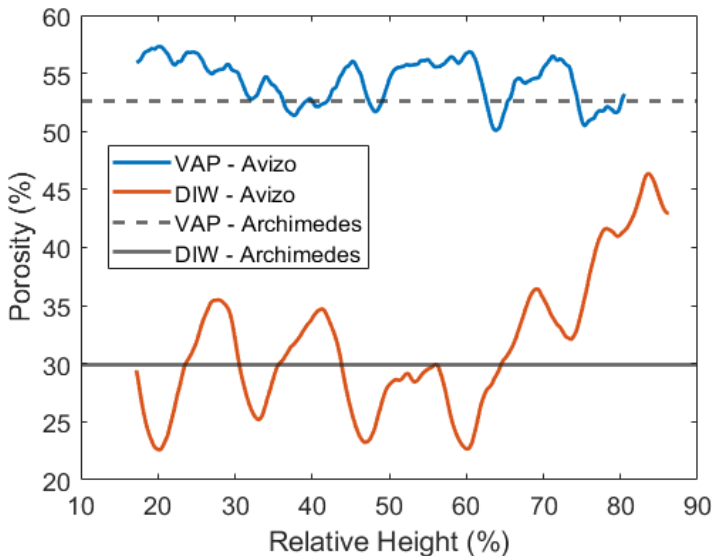

Figure 1.12. Porosity throughout the gyroid infill samples. $\sigma_{VAP} = 1.88\%$, $\sigma_{DIW} = 5.97\%$.

1.3.5 Summary

Table 1.1 compares the performance of the VAP and DW printers, according to the various results from the tests performed in this study. The nozzle diameter is primarily limited by the viscosity of the material. Since the VAP was designed to extrude highly viscous materials, it can extrude clay through a smaller nozzle diameter than can DW methods. The use of a smaller nozzle diameter consequently improves the resolution of print features, a valuable result for applications producing

millimeter-scale objects. However, the localized partial liquidation induced by the VAP's ultrasonic vibrations limits its ability to print overhangs greater than ~70°, in contrast to DW. It is worth noting, though, that the VAP can print a loose framework, and thus bridge short distances, without deforming. In this study we demonstrated that VAP could print samples with gyroid internal geometries whose porosities are shown to vary less than the DW print counterparts across the length of the sample. In addition, the higher flow momentum seen in VAP extrusion allows print speeds that are quite fast (up to 6000 mm/min) for an extrusion-based AM method. These speeds are shown to be on average 60x greater than those of a DW when extruding the clay material considered.

Table 1.1. Ranking of different print characteristics for the VAP and DIW printers. Note: the scores given are only applicable to clay extrusion. More marks equate to a more favorable comparison.

Characteristic	**VAP**	**DIW**
Nozzle diameter	XX	
Print speed	XXX	
Print resolution	X	
Porosity consistency	X	
Flow turning	X	
Overhang		X
Sagging		XX

More broadly, the performance of VAP over DW can be largely attributed to its printing mechanism. By applying intense vibrations at the syringe nozzle tip, the VAP is able to minimize the effects of wall friction on the material, hence decreasing the backpressure required for extrusion. Since extrusion is highly dependent on this backpressure, the VAP can extrude clay much more easily than this DW printer can.

1.4 Concluding Observations

This study compared the capabilities of a commercial printer using a direct-write head and a VAP printer, with particular emphasis on print quality and shape fidelity. The VAP printer demonstrated a considerable advantage over the commercial one in handling high-viscosity clay. First, the VAP

could extrude the clay through a smaller nozzle diameter than the DW print head could. This advantage enabled the VAP to produce samples with finer feature resolution and a smoother surface finish than the commercial one. Although the DW samples demonstrated consistent shape quality and the VAP had occasional issues with layer inconsistencies, the VAP's fine nozzle diameter resulted in a better overall shape quality than the DW. In addition, the VAP proved better able to print clean corners relative to the DW. Attempting sharp turning angles with the commercial printer resulted in bulges. In contrast, the VAP was able to produce sharp and clean corners.

An additional advantage demonstrated by the VAP was in overall printing speed. The commercial DW printer could not print clay at a higher head velocity than 100 mm/min, while the VAP used velocities on the order of 5-6000 mm/min. This increase in print speed drastically decreases the necessary time to print highly viscous materials. Surprisingly, although dependent on the model, it was common to observe an increase in overall print quality at higher speeds when using VAP.

The principal disadvantage of the VAP relative to the commercial DW was in overhang. The VAP process decreased the local viscosity of the clay at the nozzle exit such that unsupported lines of ink sagged or broke. In contrast, the DW method produced wide unsupported bridges in this study, as well as steeply angled unsupported wall faces. The VAP was unable to print unsupported bridges of significant width and struggled to print unsupported overhangs greater than ~70°.

This study is limited to the extrusion of clay and confirms only that VAP can easily extrude shear-thinning pastes of high viscosity, as opposed to DW methods. This work encourages the use of VAP to extrude pastes such as ceramic or propellant slurries, but has some limitations. Although highly-loaded composite slurries are generally less viscous than clay, they are also less homogeneous, making the extrusion process more difficult. For instance, composite propellant slurries are made with coarse (~200 μm) and fine particles as well as a cross-linking component (a curative), while Sculpey clay is composed of fine particles which have minimal impact on nozzle blockage. This study also does not consider the effect of varying the solids loading of the paste and does not take into account extruding materials characterized by other viscosity regimes (i.e. shear-thickening). Future works will investigate extruding propellant slurries to gauge how VAP performs with these mixtures and will explore the burning characteristics of unique AM infill

geometries. The effect of viscosity and particle distribution on print characteristics should also be quantified.

1.5 References

[1] A. Shen, C. P. Bailey, A. W. K. Ma, and S. Dardona, "UV-assisted direct write of polymer-bonded magnets," *J. Magn. Magn. Mater.*, vol. 462, pp. 220–225, 2018.

[2] A. Shen, X. Peng, C. P. Bailey, S. Dardona, and A. W. K. Ma, "3D printing of polymer-bonded magnets from highly concentrated, plate-like particle suspensions," *Mater. Des.*, vol. 183, p. 108133, 2019.

[3] Z. Chen *et al.*, "3D printing of ceramics: A review," 2019.

[4] N. V. Muravyev, K. A. Monogarov, U. Schaller, I. V. Fomenkov, and A. N. Pivkina, "Progress in Additive Manufacturing of Energetic Materials: Creating the Reactive Microstructures with High Potential of Applications," *Propellants, Explosives, Pyrotechnics*. Wiley-VCH Verlag, 2019.

[5] R. A. Chandru, N. Balasubramanian, C. Oommen, and B. N. Raghunandan, "Additive manufacturing of solid rocket propellant grains," *J. Propuls. Power*, vol. 34, no. 4, pp. 1090–1093, 2018.

[6] F. Yildirim, "OPTIMAL PROPELLANT GRAIN GEOMETRY DESIGN FOR LARGE CALIBER PROJECTILES."

[7] W. Li, A. Ghazanfari, M. C. Leu, and R. G. Landers, "Extrusion-on-demand methods for high solids loading ceramic paste in freeform extrusion fabrication," *Virtual Phys. Prototyp.*, vol. 12, no. 3, pp. 193–205, 2017.

[8] I. E. Gunduz, M. S. McClain, P. Cattani, G. T. C. Chiu, J. F. Rhoads, and S. F. Son, "3D printing of extremely viscous materials using ultrasonic vibrations," *Addit. Manuf.*, vol. 22, no. March, pp. 98–103, 2018.

[9] M. S. McClain, I. E. Gunduz, and S. F. Son, "Additive manufacturing of ammonium perchlorate composite propellant with high solids loadings," *Proc. Combust. Inst.*, vol. 37, no. 3, pp. 3135–3142, 2019.

[10] L. Rebaioli and I. Fassi, "A review on benchmark artifacts for evaluating the geometrical performance of additive manufacturing processes," *Int. J. Adv. Manuf. Technol.*, vol. 93, no. 5–8, pp. 2571–2598, Nov. 2017.

[11] Y. Ke-xi, T. Ze-ming, and W. Guo-juan, "Viscosity Prediction," *Propellants, Explos. Pyrotech.*, vol. 11, no. 6, pp. 167–169, 1986.

[12] H. L. Brooks, A. E. W. Rennie, T. N. Abram, J. McGovern, and F. Caron, "Variable Fused Deposition Modelling - Analysis of benefits, concept design and tool path generation," *Innov. Dev. Virtual Phys. Prototyp. - Proc. 5th Int. Conf. Adv. Res. Rapid Prototyp.*, pp. 511–517, 2012.

[13] "The jolly 3D printing torture-test" 2021. Available: http://www.3dbenchy.com/.

[14] P. Sehgal, M. Ramaswamy, I. Cohen, and B. J. Kirby, "Using Acoustic Perturbations to Dynamically Tune Shear Thickening in Colloidal Suspensions," *Phys. Rev. Lett.*, vol. 123, no. 12, p. 128001, 2019.

2. ISOCONVERSIONAL POWER LAW METHOD OF OBTAINING KINETIC PARAMETERS APPLIED TO THE DECOMPOSITION OF DIETHYLENE GLYCOL DINITRATE

2.1 Introduction

Condensed phase decomposition has been studied by many, and techniques have been applied to a variety of solid and liquid materials [1]–[6]. These processes are often analyzed by differential scanning calorimetry (DSC) and thermogravimetric analysis (TGA) methods with the goal to determine the kinetic parameters of the decomposition process. However, often times, the decomposition mechanism changes and occurs in multiple steps. To address the multi-step kinetics of decomposition, isoconversional methods have been developed. Isoconversional methods assume make two basic assumptions [7].

1) The rate of the decomposition process in condensed state is a function of temperature and conversion
2) This rate can be mathematically expressed by the product of two functions, which depend only on temperature and conversion, respectively

$$\frac{d\alpha}{dt} = \varphi(T,\alpha) = k(T)f(\alpha) \tag{2}$$

Where $k(T)$ is the rate constant of the reaction and $f(\alpha)$ is a function which describes the mechanism of the process. The conversion α is defined as $(m_0 - m(t))/(m_0 - m_f)$, where m_0 and m_f are the sample's starting and mass final mass, respectively. In general, an Arrhenius form of the rate constant is assumed, where $k(T) = Ae^{-E/RT}$. By integration of equation 1, the change in conversion of the sample when the temperature is raised *at a constant heating rate* can be obtained, as follows:

$$g(\alpha) = \int_{\alpha_0}^{\alpha} \frac{d\alpha}{f(\alpha)} \tag{3}$$

Where $g(\alpha)$ is also known as the integral form of the reaction mechanism $f(\alpha)$.

However, when an Arrhenius form is assumed, the solution to $g(\alpha)$ is no longer a closed form expression.

$$g(\alpha) = \int_{\alpha_0}^{\alpha_p} \frac{d\alpha}{f(\alpha)} = \frac{A}{\beta} \int_{T_0}^{T} e^{-\frac{E}{RT}} dT = h\left(Ei\left(-\frac{E}{RT}\right)\right) \tag{4}$$

Where Ei is the exponential integral and, defined on the complex plane, and h is the function resulting from the integration. In order to address such result, isoconversional and model-fitting methods must either make assumptions about the decomposition process or the reaction order, or approximate the function h, or the exponential integral itself. This raises the concerns about the implications of assuming an Arrhenius form of the rate constant, as well as the meaning behind the activation energy and Arrhenius pre-factor in in the decomposition of condensed phase materials.

Viazovkin [8] and Simon [7] address the theoretical aspects of these concerns well. The activation energy of any given reaction is the minimum energy required for the reactions to undergo the reaction. In the gas phase, the kinetics of reactions are extremely fast, and the rate of the overall reaction can often be described by a single activation energy and pre-factor. The problem arises when investigating slow condensed phase processes (i.e. liquid or solid phase decomposition). These processes are characterized by multi-step kinetics, where multiple reactions occur, each at different rates. These kinetics show strong dependence of the activation energy on temperature and the conversion of the material. To add complexity, in a solid medium, the reaction step can occur at different rates based on the spatial location in the medium due to restricted molecular motion in the solid [8]. Similarly, in a liquid medium, the dielectric properties of the liquid play a role, and the activation energy has been shown to depend on the viscosity of the material, which is also often temperature dependent. Even in relatively fast condensed phase processes, such as the combustion of solid propellants, there are errors when approximating the reaction as a single-step process.

Consequently, the Arrhenius kinetic parameters have little physical meaning for condensed phases. The parameters can be seen as fitting parameters, or as quantities determined by empirical factors rather than theory. In other words, the Arrhenius activation energy in condensed phase decomposition processes is somewhat similar to the role that phenomenological parameters such as the convection coefficient has in heat transfer.

To validate the above statement, this study aims to assume a form of the rate constant that is different from the Arrhenius form. Generally, the objectives of this study are as follows:

1) To derive an isoconversional model based on assuming a power law rather than an Arrhenius form for the rate constant
2) Apply the method to analyze the decomposition of DEGDN and compare the results to pre-existing methods
3) Assess the validity of the new isoconversional method

2.2 Methods

2.2.1 Materials

Diethylene glycol dinitrate (DEGDN) is an energetic plasticizer that can potentially be used in double base propellant formulations. Specifically, the plasticizer is seen as a replacement to nitroglycerin (NG) in medium to large caliber gun systems because of its energetic content and improved sensitivity [9]–[12]. However, in the open literature, differential scanning calorimetry (DSC) and thermogravimetric analysis (TGA) have not been performed on DEGDN, and its decomposition kinetics are unknown.

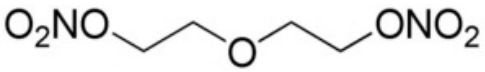

In this study, the plasticizer is synthesized in a laboratory environment and stabilized in isopropanol. Prior to testing, the stabilized DEGDN is stored in a dry environment for 120 hours in order to evaporate the isopropanol.

2.2.2 Thermal Analysis

DEGDN samples of 3 mg were used throughout the study. The samples were placed in a DSC-TGA analyzer (TA Instrument Q600 SDT) in an argon environment using a flow rate of 90 mL/min. The samples were contained in alumina pans. The samples were subjected to a 10 minute isothermal at 298 K followed by ramped heating until 573 K. Heating rates of 2, 5, 10 and 20 K/min were used.

2.2.3 Isoconversional Power Law Model Derivation

Commonly, thermal decomposition is described by the following overall reaction

$$R\left(\frac{solid}{liquid}\right) \rightarrow P\left(\frac{solid}{liquid}\right) + P\left(\frac{volatile}{gases}\right) \tag{5}$$

where R are the reactants, whether solid or liquid, and P are the product. The decomposition rate ($d\alpha/dt$) for the above reaction at temperature T is described by equation 5. The assumed power law in the form of $k(T) = A_p T^m$ is substituted. We can substitute $d\alpha/dt = \beta \cdot d\alpha/dT$ in order to arrive to an integrable form with respect to temperature. Of course, the following is only valid for constant heating rates.

$$\frac{d\alpha}{dt} = A_p T^m f(\alpha) = \frac{A_p}{\beta} T^m f(\alpha) \tag{6}$$

From the definition of $g(\alpha)$, we obtain a solution to the closed form integral, as follows.

$$g(\alpha) = \int_{\alpha_0}^{\alpha} \frac{d\alpha}{f(\alpha)} = \frac{A_p}{\beta} \int_{T_0}^{T} T^m dT = \frac{A_p}{\beta(m+1)} T^{m+1} \tag{7}$$

By rearranging the equation for β and taking logarithms of each side, we arrive to the following form of the model, tantamount to the line formula $y = b + (dy/dx)x$.

$$\log \beta = \log\left(\frac{A_p}{g(\alpha)(m+1)}\right) + (m+1)\log T \tag{8}$$

By using this form, the values of $\log(\beta)$ can be plotted against those of $\log(T)$, where T is defined as the temperature at a specified conversion factor. The power coefficient m can be found from the slope of the line, and the power pre-factor can then be solved for, as follows.

$$A_p = e^b g(\alpha)(m+1) \tag{9}$$

where b is the y-intercept of the line.

Although the following step is not necessary, for the sake of comparison, the activation energy and Arrhenius pre-factor can be obtained by fitting the power law to the Arrhenius equation. This is done by calculating a set of rate constants within the range of temperatures tested, and plotting $\ln\big(k(T)\big)$ against $1/T$. The slope of the line is equal to E/R and its y-intercept is equal to $\ln(A)$.

$$\ln k(T) \equiv \ln A_p + m \ln T \leftrightarrow \ln A - \frac{E}{RT} \tag{10}$$

It is worth mentioning that many other forms of the rate constants can be assumed as long as a closed form solution to the integral can be solved for. The activation energy and pre-factor could then be solved in a similar manner to that shown here.

2.2.4 Criado's Method

In this study, Criado's method is also used to find the kinetic model of the decomposition process of DEGDN. The method works by generating a master curve of common reaction mechanisms, and then assessing which curve the decomposition most closely follows [13], [14]. The following (normalized) equation is used:

$$\frac{Z(\alpha)}{Z(0.5)} = \frac{f(\alpha)g(\alpha)}{f(0.5)g(0.5)} = \left(\frac{T_\alpha}{T_{0.5}}\right)^2 \frac{(d\alpha/dt)_\alpha}{(d\alpha/dt)_{0.5}} \tag{11}$$

Where the subscript '0.5' refers to values at a conversion factor $\alpha = 0.5$, T_α is the temperature at a specified conversion factor, and $(d\alpha/dt)_\alpha$ is the rate of change of the conversion factor.

The left hand side of the equation is used to generate a theoretical curve for each reaction mechanism, while the right hand side is used to plot the reduced rate associated with experimental data.

The chosen reaction mechanism is used throughout the rest of this study to determine $g(\alpha)$ and hence the kinetic parameters. In order to choose an appropriate model, Spearman's correlation coefficient was computed to compare the experimental curve to each of the theoretical curves. Spearman's method assesses monotonic (linear and non-linear) relationships between curves as per equation 11.

$$\rho = 1 - \frac{6\sum d_i^2}{N(N^2-1)} \tag{12}$$

Where ρ is the spearman correlation coefficient, N is the number of data points collected during the experiment, and d_i is the difference between the two ranks of each observation

The model with the highest Spearman coefficient is then chosen. For completeness, table 2.1 shows the many reaction mechanisms evaluated.

Table 2.1. Reaction mechanisms function used in the analysis of DEGDN decomposition (adapted from [14]).

Mechanism	$f(\alpha)$	$g(\alpha)$
Power law (P2)	$2\alpha^{1/2}$	$\alpha^{1/2}$
Power law (P3)	$3\alpha^{3/4}$	$\alpha^{1/3}$
Power law (P4)	$4\alpha^{3/4}$	$\alpha^{1/4}$
Avarami-Erofe've (A2)	$2(1-\alpha)[-\ln(1-\alpha)]^{1/2}$	$[-\ln(1-\alpha)]^{1/2}$
Avarami-Erofe've (A3)	$3(1-\alpha)[-\ln(1-\alpha)]^{2/3}$	$[-\ln(1-\alpha)]^{1/3}$
Avarami-Erofe've (A4)	$4(1-\alpha)[-\ln(1-\alpha)]^{3/4}$	$[-\ln(1-\alpha)]^{1/4}$
Contracting sphere (R2)	$2(1-\alpha)^{1/2}$	$[1-(1-\alpha)^{1/2}]$
Contracting sphere (R3)	$3(1-\alpha)^{2/3}$	$[1-(1-\alpha)^{1/3}]$
One-dimensional diffusion (D1)	$1/2\alpha$	α^2
Two-dimensional diffusion (D2)	$[-\ln(1-\alpha)]^{-1}$	$(1-\alpha)\ln(1-\alpha)+\alpha$
Three-dimensional diffusion, Jander (D3)	$3(1-\alpha)^{2/3}\ /[2(1-(1-\alpha)^{1/3})]$	$\left[1-(1-\alpha)^{1/3}\right]^2$
Ginstling-Brounshtein (D4)	$3/2((1-\alpha)^{-1/3}-1)$	$1-(2\alpha/3)-(1-\alpha)^{2/3}$
First-order (F1)	$1-\alpha$	$-\ln(1-\alpha)$
Second-order (F2)	$(1-\alpha)^2$	$(1-\alpha)^{-1}-1$
Third-order (F3)	$(1-\alpha)^3$	$[(1-\alpha)^{-2}-1]/2$

2.2.5 Isoconversional and Model-Fitting Methods

In order to properly assess the validity of using a power law to obtain kinetic parameters, the model is thoroughly compared to a multitude of isoconversional and model-fitting methods. A summary of these models as well as their sources of error can be found in Table 2.2. References to the original papers of each model are also listed in Table 2.2 should the reader be interested. In addition, the International Confederation for Thermal Analysis and Calorimetry (ICTAC) does a remarkable job of explaining many of the models outlined this study [15].

The Ozawa-Flynn-Wall model has been widely used to determine kinetic parameters of polymers, energetics and many other types of materials [14], [16]–[19]. The main assumption to the model is that the reaction mechanism $f(\alpha)$ is independent of changes in the heating rates. Since the model assumes an Arrhenius form of the rate constant, the evaluation of the function $\log(p(u))$ uses Doyle's approximation, which is a series approximation of the exponential integral [20]. Similarly, the Kissinger-Akahira-Sunose model is based on the Murray and White approximation of the integral. Friedman's method, on the other hand, simply takes the logarithms of equation 1 where $k(T)$ assumes an Arrhenius form. Hence, the accuracy of the method is highly dependent on the noise in the $d\alpha/dt$ curve. In contrast to the above methods, the Vyazovkin method is newer and uses numerical integration to determine the activation energy. The method follows the transition

state theory, where the pre-factor is independent of the activation energy, and A is simply a scaling factor for the overall reaction rate. More importantly, the method attempts to capture a single value of activation energy and pre-factor in order to model the overall reaction rate of the decomposition process.

Table 2.2. Summary of thermal analysis models used to determine kinetic parameters.

Model	Estimation of E and A	Assumptions/Sources of Error	Reference
Afriat (Power Law)	$\log\beta = \log\left(\frac{A_p}{g(\alpha)(m+1)}\right) + (m+1)\log T$	Source of error present if fitting power law to another form (i.e. Arrhenius)	This work
Ozawa-Flynn-Wall	$\log\beta = \log\left(\frac{AE}{g(\alpha)R}\right) + \log(p(u))$	$\log(p(u)) \cong -2.315 - 0.4567(u)$	[17]
Kissinger-Akahira-Sunose	$\ln\left(\frac{\beta}{T^2}\right) = \ln\left(\frac{AR}{Eg(\alpha)}\right) - \frac{E}{RT}$	$p(u) \cong \frac{e^{-u}}{(u)^2}$	[21]
Friedman	$\ln\left(\frac{d\alpha}{dt}\right) = \ln(f(\alpha)A) - \frac{E}{RT}$	Highly sensitive to $d\alpha/dt$ variability	[22]
Vyazovkin	$\mathrm{E}\left(\frac{\mathrm{d}\Phi}{\mathrm{dE}} = 0\right), \quad \log A = C_1\bar{E} + C_2$	Numerical integration error	[23]
Coats-Redferns	$\ln\left(\frac{g(\alpha)}{T^2}\right) = \ln\left[\left(\frac{AR}{\beta E}\right)\left(1 - \frac{2R\bar{T}}{E}\right)\right] - \frac{E}{RT}$	$\int_u^\infty e^{-u}du \cong u^{-1-b}e^{-u}\sum_{n=0}^{\infty}\frac{(-1)^n b^n}{u^{n+1}}$	[24]
Augis-Bennett	$\ln\left(\frac{\beta}{T-T_0}\right) = \ln A - \frac{E}{RT}$	• $A^w e^{-wE/RT} \cong \left(\frac{T-T_o}{\alpha}\right)^{-w}, w = 1$ • $\frac{E}{R}\frac{T-T_o}{T^2} \gg 1$	[25]
Kissinger	$\ln\left(\frac{\beta}{T^2}\right) = \ln\left(\frac{AR}{E}\right) - \frac{E}{RT}$	• $f(\alpha) = (1-\alpha)^w, w = 1$ • $\frac{d^2\alpha}{dT^2} = 0 \; at \; T = T_m$	[26]
Borchardt-Daniels	$\ln\left(\frac{d\alpha}{dt}\right) - w\ln(1-\alpha) = \ln A - \frac{E}{RT}$	$\frac{d\alpha}{dt} = k(T)(1-\alpha)^w$	[27]

Note. $\bar{E}$ is the average activation energy obtained over the range of α, $\bar{T}$ is the average temperature of the sample, T_0 is the onset temperature of the TGA curve, w is the order of reaction based on the reaction mechanism, and also acts a fitting parameter in the Borchardt-Daniels equation. Also, $u = E/RT$.

2.3 Results

2.3.1 Thermal Analysis

The results of the DSC TGA experiments are shown in figure 1 and the relevant temperature and mass loss values are summarized in table 2.3. Throughout the experiments, the DEGDN did not exhibit any unexpected or irregular behavior. The DSC shows that a strictly exothermic reaction takes place during the decomposition of DEGDN, with only one exothermic peak to report each run. As the heating rate increases, the area under the heat flow versus temperature curve increases, and so does the peak heat flow. Similarly, the rate of conversion (and rate of mass loss) increases

as well. As expected, the onset and endset temperatures both increase as the heating rate is increased. The total mass loss remains relatively steady at 99% - 99.39%, which indicates that nearly all of the material is consumed by the time that the final temperature (573 K) is reached.

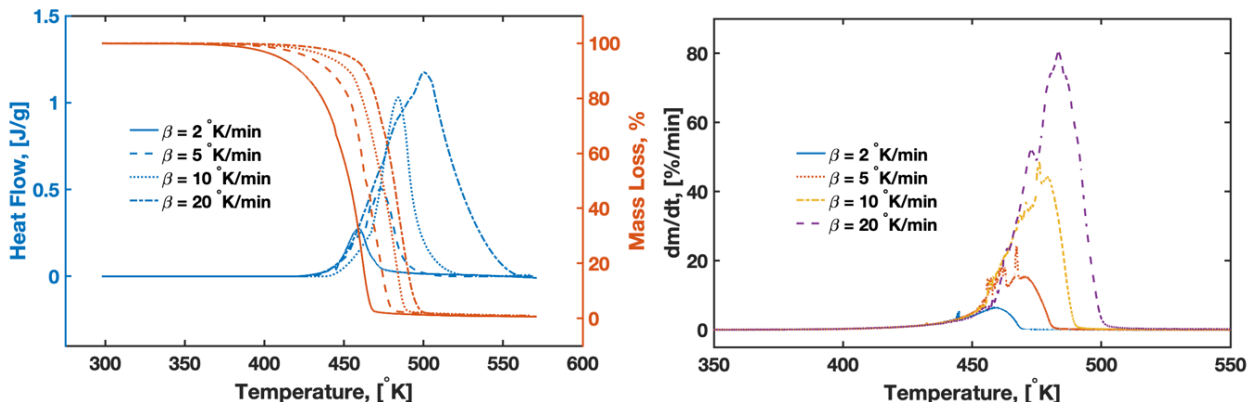

Figure 2.1. Left: DSC-TGA plot of heat flow and mass remaining versus temperature. Right: DTG plot of the derivative of mass with respect to time, as a function of temperature.

Table 2.3. Characteristic parameters of DEGDN decomposition obtained from DSC-TGA analysis.

	TGA			DTG		DSC
$\beta\left[\frac{K}{min}\right]$	T_{ot} $[K]$	T_{es} $[K]$	$Mass\ loss$ $[\%]$	T_p $[K]$	T_{oe} $[K]$	T_{od} $[K]$
2	430.1	466.8	99.39	462.9	469.4	426.8
5	450.3	479.1	99.04	467.2	480.5	436.6
10	455.6	487.8	99.0	484.7	489.9	444.2
20	462.0	495.6	99.30	483.4	500.1	445.7

Note. DTG is the rate of mass loss curve, T_{ot} is the onset temperature of decomposition, T_{es} is the endset temperature, T_p is the temperature at peak mass loss rate, T_{oe} is the endset temperature of the mass loss rate curve, and T_{od} is the onset temperature of the DSC curve

In addition to heat flow and the sample's change in mass over time, it is important to visualize the effects of self-heating. As described above, isoconversional models are derived using constant heating rates. While a constant heating rate is programmed in the DSC TGA experiments, the actual heating rate varies as the temperature approaches the exotherm (figure 2.2). The exothermic reactions induce a rapid change in heat output, which changes the sample temperature. The changes in temperature and heating rate over time are calculated using equations 12 and 13. As seen in figure 2.2, the actual heating rate can change from 20 K/min to a maximum of 26 K/min, which may induce errors in the calculation of kinetic parameters.

$$\delta T = T_{ac}(t) - T_{prog}(t) \tag{13}$$

$$\delta\beta = \beta_{ac}(t) - \beta_{prog} = \frac{dT}{dt}(t) - \beta_{prog} \tag{14}$$

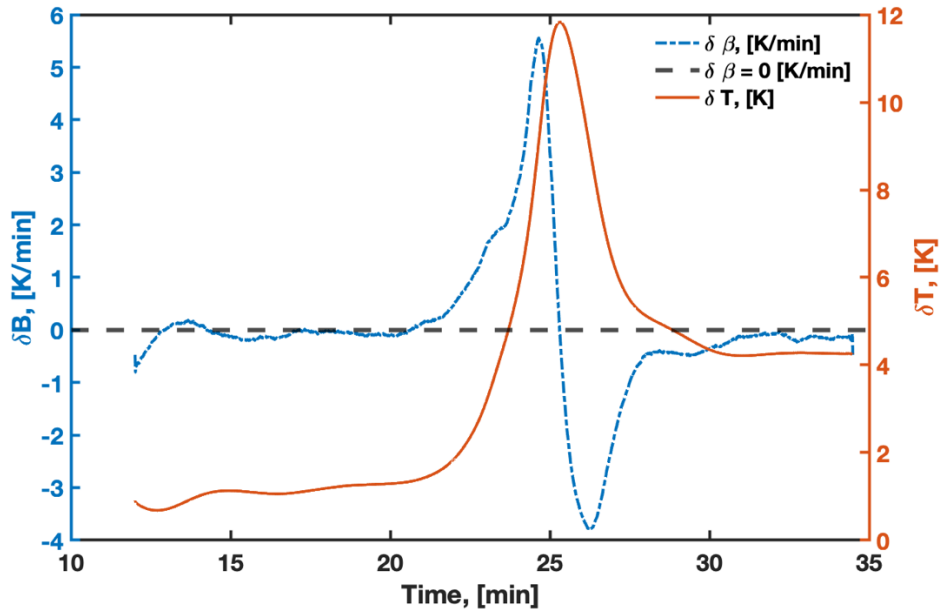

Figure 2.2. Self-heating effect occurring during non-isothermal decomposition of DEGDN. β = 20 K/min.

2.3.2 Decomposition Reaction Mechanism

As for many nitrate esters, the initial decomposition of the DEGDN (and its rate-determining step) can be characterized by the hydrolysis of the $O - NO_2$ bond, which may a reversible process [28].

$$RCH_2O - NO_2 \leftrightarrow RCH_2O \cdot + NO_2 \cdot$$

According to the analysis performed using Criado's method, DEGDN decomposition follows the Avarami-Erofe've (A3) model, with a high Spearman coefficient ρ = 0.90 (figure 2.3). The decomposition of DEGDN is therefore a third order (n = 3) sigmoidal mechanism. In other words, the initial stage of the decomposition accelerate the rate of reaction until a maximum reaction rate is reached, while the final stages exhibit a decelerating behavior. (See [29] for further detail on the A3 model and nucleation theory in solid state reactions). Although many materials and polymers (i.e. nitrocellulose and polyvinyl nitrate [30]) exemplify multiple reaction mechanisms during decomposition, the decomposition of DEGDN can reasonably be characterized as third order throughout.

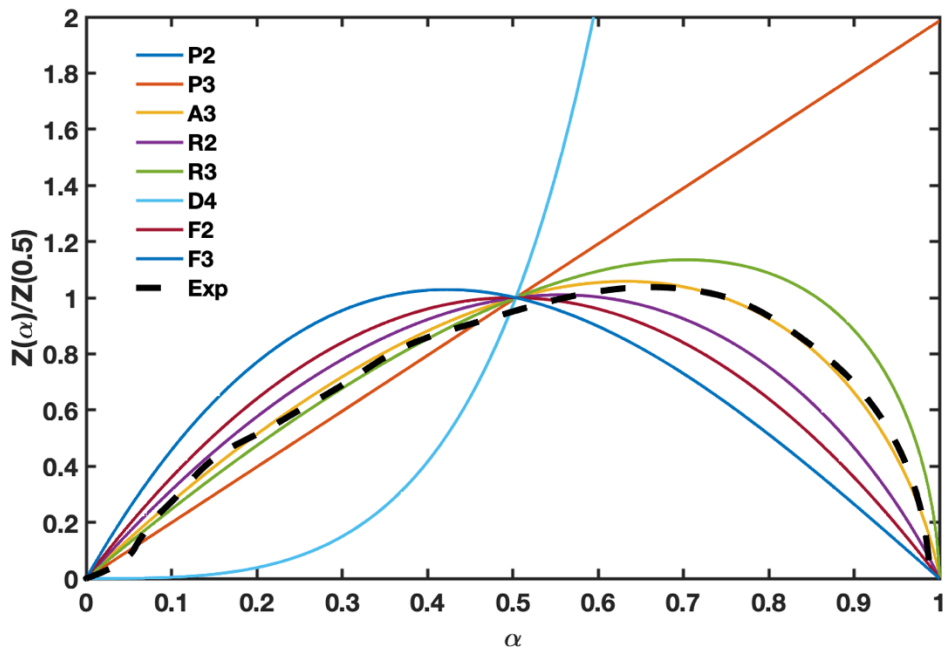

Figure 2.3. Master curve of multiple reaction mechanisms and experimental curve at a heating rate of 20 K/min for DEGDN using Criado's method. For clarity, 8 out of the 15 models analyzed are displayed here.

2.3.3 Isoconversional Power Law

The power law method outlined above can be graphically represented (figure 2.4). In order to get the power law parameters (coefficient A_p and exponent m) a plot of $\log \beta$ vs $\log T$ is generated. As for other isoconversional models, the more experiments are conducted, the more points can be plotted and a higher confidence fit can be obtained. Once the power law parameters are obtained, the rate constant $\log k(T)$ is calculated at various temperatures and plotted against $1/T$, where the activation energy and Arrhenius pre-factors can be obtained.

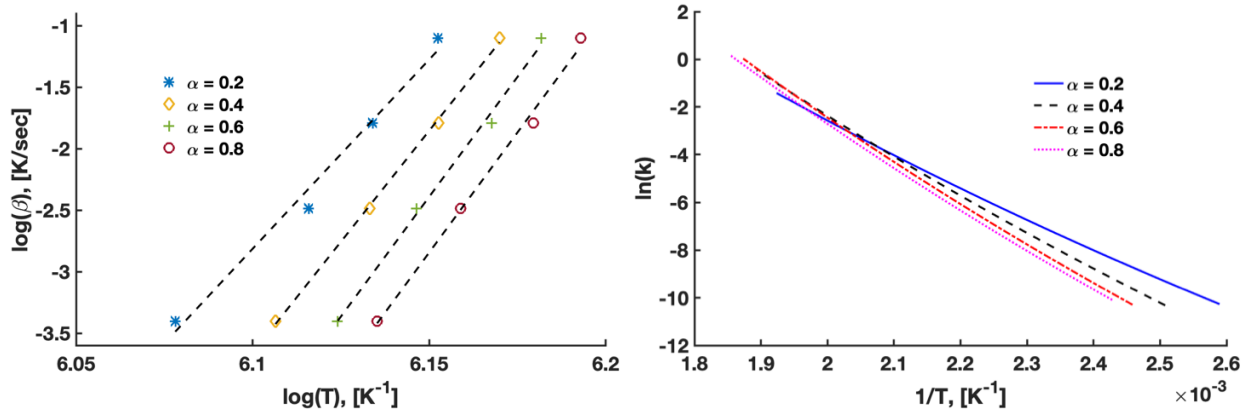

Figure 2.4. Left: Plot of logarithms of heating rate versus the logarithms of temperature for indicated conversions of the decomposition of DEGDN. Right: Arrhenius plot obtained from the power law parameters at indicated conversions of the decomposition of DEGDN.

The activation energy and pre-factor are then compared to a variety of isoconversional and model-fitting methods. These kinetic parameters were evaluated at 25 conversion factors, all of which are plotted in figure 2.5. The Afriat (power law) method exhibits activation energy values that are in excellent agreement with Ozawa-Flynn-Wall (OFW) and -Kissing-Akahira-Sunose (KAS). The activation energies using these three methods increase with conversion until $\alpha \cong 0.5$, and then stabilizes at 145-150 kJ/mol. The pre-factors using the Afriat method is also nearly equal to those obtained using OFW and KAS (table 2.4). In addition, the Friedman model shows an increasing activation energy until about $\alpha \cong 0.4$, after which the value oscilates with increasing conversion. These oscillations are caused by the variability of the time rate of change of the conversion explained in the methods section.

Furthermore, the Kissinger and Ozawa methods calculated nearly identical kinetic parameters. The Augis-Bennet (AB) method calculates a slightly higher activation energy value than do the Kissinger and Ozawa methods. This disparity is a result of the AB model taking into account the dependence of onset temperature on heating rate, where the difference between the temperature at maximum degradation and the onset temperature is relatively small. Rather interestingly, this difference is likely due to the accelerating behavior of the decomposition process as exemplified by the contracting sphere reaction mechanism.

Finally, the Vyazokin method, as it was designed, calculates activation energies that are relatively independent of conversion. The average activation energy is 193.8 kJ/mol and is 20 kJ/mol higher than that using the Augis-Bennett model.

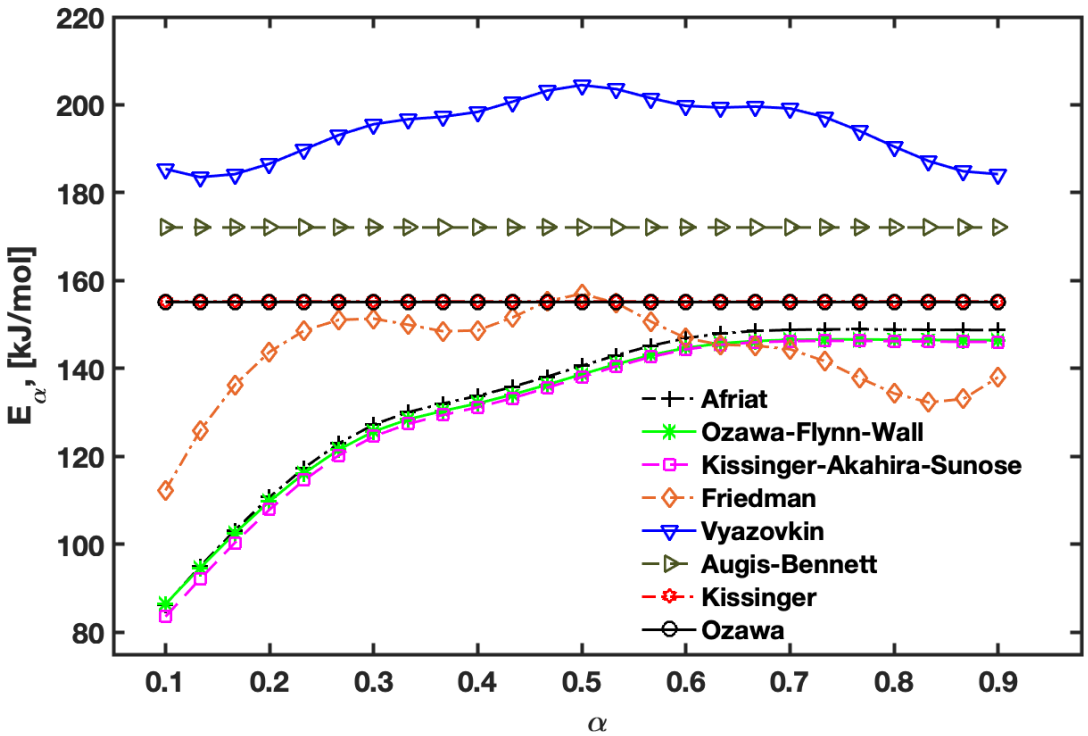

Figure 2.5. Comparison of activation energy values of DEGDN for α = [0.1 – 0.9] using the models outlined in table 2. The plot shows how Augis-Bennett, Kissinger and Ozawa models are independent of conversion factor. The Ozawa model is the conversion-independent version of the Ozawa-Flynn-Wall model.

Table 2.4. Comparison of kinetic parameters between Power Law and Ozawa-Flynn-Wall models for DEGDN decomposition.

	Power Law		Ozawa-Flynn-Wall	
α	$E_{AFR}, \left[\frac{kJ}{mol}\right]$	$\log A_{AFR}, [s^{-1}]$	$E_{OFW}, \left[\frac{kJ}{mol}\right]$	$\log A_{OFW}, [s^{-1}]$
0.1	86.32	17.63	86.4	17.75
0.2	110.75	24.0	109.8	23.68
0.3	127.24	28.25	125.7	37.72
0.4	133.79	29.80	138.7	29.23
0.5	140.61	31.43	144.7	30.80
0.6	146.90	32.91	146.5	32.20
0.7	148.81	33.27	146.5	32.54
0.8	148.89	33.16	146.6	32.43

2.3.4 Model-Free Kinetics and Compensation Effects

From the average activation energy of the Vyazovkin method, a single pre-factor can be obtained for the overall reaction by plotting a linear fit between activation energies and pre-factors obtained by Coats-Redfern's (CR) method (figure 2.6). Figure 2.7 also shows the average activation energy obtained using the CR method for each of the reaction mechanisms investigated, as well as their variability. As figure 2.6 shows, there is a clear positive linear relationship between E and log (A). This is otherwise known as the kinetic compensation effect, where an increase in activation energy does not cause a decrease in the reaction rate as log (A) increases to compensate for E [31].

The compensation effect has been observed in many solid phase decomposition reactions and under a variety of experimental conditions [31]. The activation energies and pre-factors obtained for different conversions using the Afriat model are plotted alongside the CR and Vyazovkin values. The lines of best fit obtained using Afriat method falls almost exactly on the CR line. Their slopes differ by 0.01 and theirs y-intercepts differ by 1.79. This means that if one were to know only either the activation energy or the pre-factor of a DEGDN decomposition reaction, the second kinetic parameter can be obtained by equation 14:

$$\log A\,[s^{-1}] = 0.27E\left[\frac{kJ}{mol}\right] - 7.82 \tag{15}$$

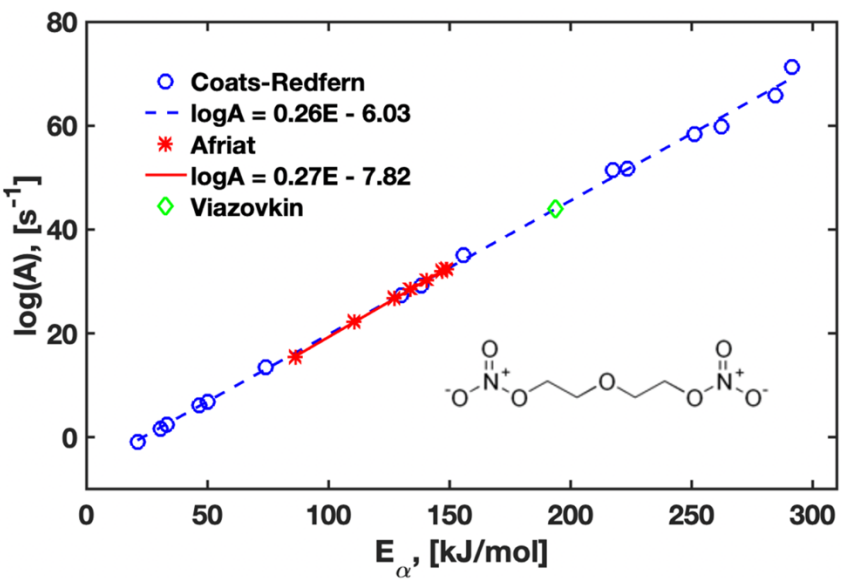

Figure 2.6. Compensation effect for the different thermal decomposition mechanisms of DEGDN

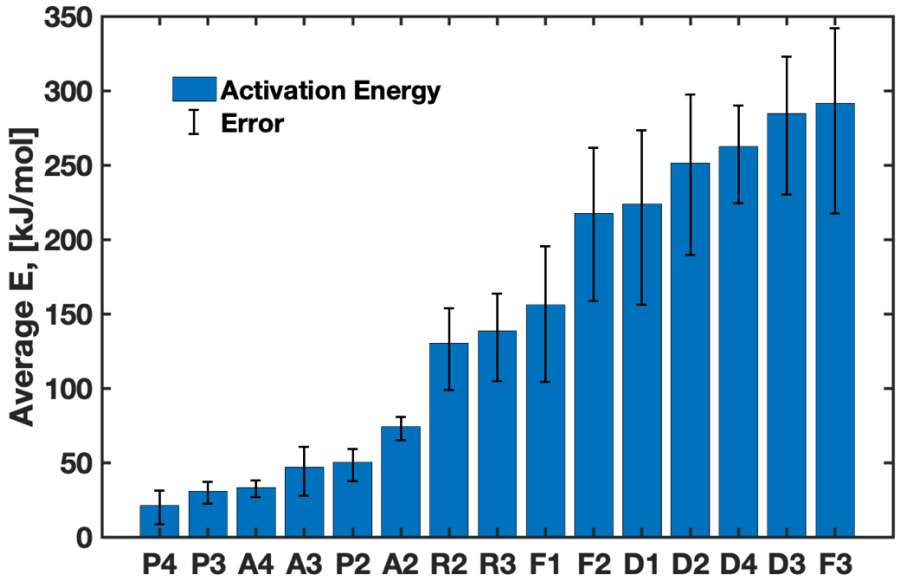

Figure 2.7. Plot of average activation energy values obtained using the Coats-Referns model for the reaction mechanisms analyzed in this paper. The analysis was performed from $\alpha = 0.2$ to $\alpha = 0.8$.

2.3.5 Lifetime of DEGDN

The ICTAC Kinetics Committee defines the lifetime of a material as "the time after which the material loses its properties to such extent that it cannot fulfill efficiently the function for which it was created [15]."

$$t_\alpha = \frac{g(\alpha)}{Aexp(-E/RT_0)} \tag{16}$$

For this study, we define the extent of decay at which the material becomes unusable as $\alpha = 0.1$, which roughly corresponds to 10-15% mass loss depending on the heating rate used. Out of four isoconversional models, the power law is the most conservative throughout the range of temperatures. The lifetime of a DEGDN (not stabilized) for $\alpha = 0.1$ is near 14 days at 298 K using the power law.

Furthermore, the lifetime was plotted at various temperature ranges as shown in figure 2.8. The Friedman model is the least conservative (highest lifetime) early in the temperature range, and becomes the most conservative at higher temperatures. Using the kinetic parameters of the OFW and KAS models, the lifetimes are nearly identical. However, it is worth mentioning that the decomposition kinetic parameters obtained in this study are applicable in the temperature range

tested (298 K – 573 K), and may change at higher temperature ranges. At the higher end of the temperature range (573 K), the power law and the Friedman models estimate the lifetime to be 50 ms. At that temperature, the fast kinetics may trigger chain reactions which could lead to ignition of DEGDN. Although that has yet to be tested, a 0-D kinetic simulation of using C, H, N, O species including kinetic parameters obtained in this paper could be performed.

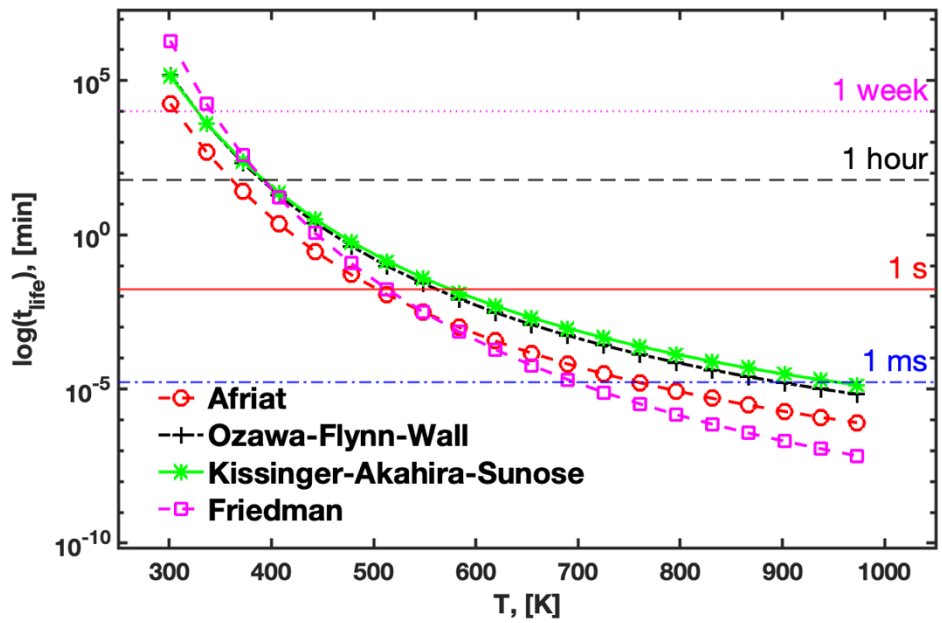

Figure 2.8. Comparison of sample lifetime for different isoconversional models, at α = 0.1.

2.3.6 Ignition Temperature of DEGDN

In order to estimate the autoignition temperature of DEGDN from, we use a formula derived by Huang and Wu [32]. The method includes the effects of self-heating of the material and makes use of Semenov's theory's condition for thermal explosion. The formula typically overestimates the autoignition temperature by 5 to15 K when compared to value obtained from small-scale cook-off experiments on energetic materials. The formula has also successfully been applied to condensed energetic mixtures.

$$T_{ign} = \frac{-\frac{E}{R}\sqrt{\left(\frac{E}{R}\right)^2 + 4\left(\frac{E}{R}\right)T}}{2} \tag{17}$$

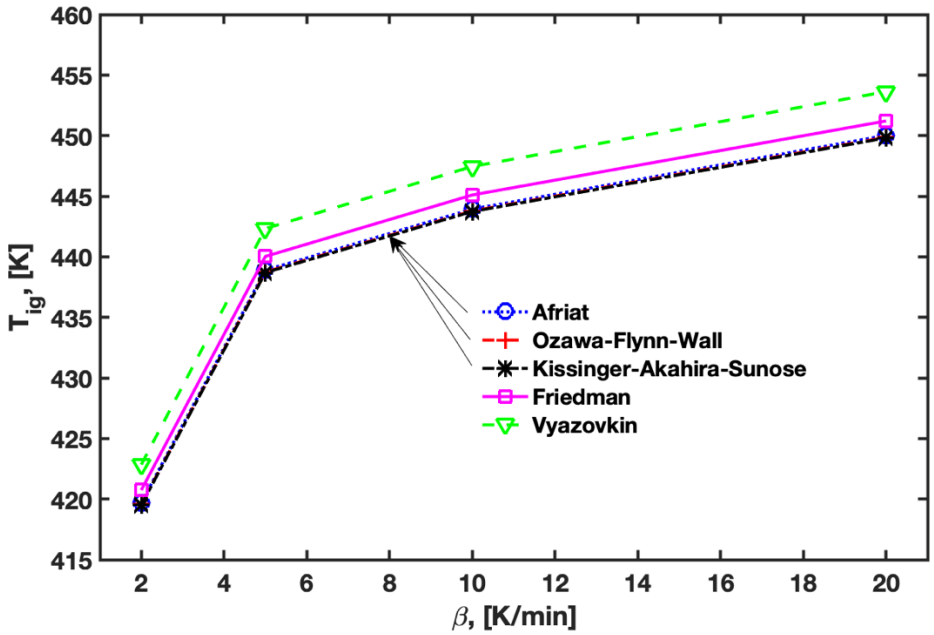

Figure 2.9. Theoretical ignition temperature of DEGDN for different heating rates for α = 0.5.

Figure 9 shows the dependence of ignition temperature on the heating rate using various methods. The Afriat, OFW and KAS methods are most conservative, showing temperatures of 420 K at 2 K/min to 450 K at 20 K/min. The temperature values obtained using these three methods are nearly identical. In comparison, owing to the higher activation energies obtained using Vyazokin and Friendman methods, the autoignition temperatures are a few degrees higher.

2.4 Discussion

The purpose of this study is not assess which isoconversional or model-fitting method is best to obtain kinetic parameters, as that is highly case-by-case dependent, and also depends on the objective of the experiment. For example, assuming one knew exactly which reactions are occurring as a function of material conversion, one could obtain the kinetic parameters of these overall reactions using isoconversional methods. On the other hand, if little to none is known about the material, then global kinetic parameters can be determined using Vyazovkin's method.

Rather, the authors hope to shine light on the meaning and the implications of the Arrhenius parameters with respect to the decomposition of condensed phase materials. These parameters are strongly dependent on the type of condensed medium, the conversion and the temperature, and

have shown to have little physical meaning to condensed phase decomposition. As it has been shown in this study, it is not necessary to assume an Arrhenius form for the rate constant in order to determine kinetic parameters. Any appropriate form, can be assumed, as long as a solution to the closed form integral can be obtained, as demonstrated in the methods section.

By using a power law isoconversional method, it was found that the activation energy and pre-factor are in excellent agreement with those using the OFW and KAS methods. These values were compared to many other methods, showing the dependence – or independence of activation energy on the conversion of DEGDN. This dependence is a result of the multi-step kinetics taking place in condensed phase decomposition. Although the kinetic parameters can vary widely under different experimental conditions (known as the compensation effect), a linear fit between the activation energy and the pre-factor can be found. As a result, a general formula has been obtained for the decomposition of DEGDN, where one can find the second kinetic parameter by knowing the other. This may help kineticists and modelers interested in the decomposition of DEGDN.

Furthermore, one of the aims of this study was to analyze the thermal decomposition of DEGDN. The DSC and TGA experiments did not exhibit any irregular behavior, and the trends in onset temperature, heat release, and mass loss rate as a function of heating rates are as expected. By using Criado's method, DEGDN decomposition exhibits a third order Avrami Erofeev (A3) mechanism. The lifetime of DEGDN was also estimate for a range of isothermal temperatures and can be used as a reference for the aging of DEGDN. The Afriat method was shown to lead the least conservative lifetime values compared to other methods. Finally, the theoretical ignition temperature was estimated at various heating rates and shows strong agreement with KAS and OFW methods.

2.5 Conclusion

In this study, a power law isoconversional method was derived and applied to the decomposition of DEGDN. The method was shown to compare excellently to other isoconversional methods such as Ozawa-Flynn-Wall and Kissinger-Akahira-Sunose. The method was also compared to various both isoconversional and model-fitting methods to obtain a range of

kinetic parameters of DEGDN. Using these values, the autoignition temperature was obtained as a function of heating rate, as well as the material's lifetime.

2.6 References

[1] B. Janković, N. Manić, and D. Stojiljković, "The gaseous products characterization of the pyrolysis process of various agricultural residues using TGA–DSC–MS techniques," *J. Therm. Anal. Calorim.*, vol. 139, no. 5, pp. 3091–3106, 2020.

[2] S. Vyazovkin, J. S. Clawson, and C. A. Wight, "Ammonium Nitrate RT)," no. 19, pp. 960–966, 2001.

[3] S. Matečić Mušanić, I. Fiamengo, and M. Sućeska, "Determination of Nitroglycerine Content in Double Base Propellants by Isothermal Thermogravimetry," *Cent. Eur. J. Energ. Mater.*, vol. 7, no. 1, pp. 3–19, 2010.

[4] M. Abd-Elghany, A. Elbeih, and T. M. Klapötke, "Thermo-analytical study of 2,2,2-trinitroethyl-formate as a new oxidizer and its propellant based on a GAP matrix in comparison with ammonium dinitramide," *J. Anal. Appl. Pyrolysis*, vol. 133, no. April, pp. 30–38, 2018.

[5] C. P. Lin, Y. M. Chang, J. P. Gupta, and C. M. Shu, "Comparisons of TGA and DSC approaches to evaluate nitrocellulose thermal degradation energy and stabilizer efficiencies," *Process Saf. Environ. Prot.*, vol. 88, no. 6, pp. 413–419, 2010.

[6] L. Müller, G. Rubio-Pérez, A. Bach, N. Muñoz-Rujas, F. Aguilar, and J. Worlitschek, "Consistent DSC and TGA methodology as basis for the measurement and comparison of thermo-physical properties of phase change materials," *Materials (Basel).*, vol. 13, no. 20, pp. 1–20, 2020.

[7] P. Šimon, "Isoconversional methods: Fundamentals, meaning and application," *J. Therm. Anal. Calorim.*, vol. 76, no. 1, pp. 123–132, 2004.

[8] S. Vyazovkin, "On the phenomenon of variable activation energy for condensed phase reactions," *New J. Chem.*, vol. 24, no. 11, pp. 913–917, 2000.

[9] D. A. Reese, L. J. Groven, and S. F. Son, "Formulation and characterization of a new nitroglycerin-free double base propellant," *Propellants, Explos. Pyrotech.*, vol. 39, no. 2, pp. 205–210, 2014.

[10] S. Chaturvedi and P. N. Dave, "Solid propellants: AP/HTPB composite propellants," *Arab. J. Chem.*, vol. 12, no. 8, pp. 2061–2068, 2019.

[11] S. Sun, S. Ma, B. Zhao, G. Zhang, and Y. Luo, "A facile way to prolong service life of double base propellant," *Materials (Basel).*, vol. 11, no. 11, 2018.

[12] I. Thelma, M. Montville, P. Joseph, B. Lake, S. Moy, and N. J, "PATENT: HIGH ENERGY TNAZ, NITROCELLULOSE GUN PROPELLANT," no. 19, pp. 3–5, 1998.

[13] J. M. Criado, "Kinetic analysis of DTG data from master curves," *Thermochim. Acta*, vol. 24, no. 1, pp. 186–189, 1978.

[14] A. Aboulkas, K. El, and A. El Bouadili, "Thermal degradation behaviors of polyethylene and polypropylene . Part I : Pyrolysis kinetics and mechanisms," *Energy Convers. Manag.*, vol. 51, no. 7, pp. 1363–1369, 2010.

[15] S. Vyazovkin, A. K. Burnham, J. M. Criado, L. A. Pérez-Maqueda, C. Popescu, and N. Sbirrazzuoli, "ICTAC Kinetics Committee recommendations for performing kinetic computations on thermal analysis data," *Thermochim. Acta*, vol. 520, no. 1–2, pp. 1–19, 2011.

[16] S. Matečić Mušanić, M. Sućeska, and I. Fiamengo Houra, "Applicability of Non-isothermal DSC and Ozawa Method for Studying Kinetics of Double Base Propellant Decomposition," *Cent. Eur. J. Energ. Mater.*, vol. 7, no. 3, pp. 233–251, 2010.

[17] T. Ozawa, "A New Method of Analyzing Thermogravimetric Data," *Bull. Chem. Soc. Jpn.*, vol. 38, no. 11, pp. 1881–1886, 1965.

[18] M. Abd-Elghany, T. M. Klapötke, and A. Elbeih, "Environmentally safe (chlorine-free): New green propellant formulation based on 2,2,2-Trinitroethyl-formate and HTPB," *RSC Adv.*, vol. 8, no. 21, pp. 11771–11777, 2018.

[19] M. Abd-Elghany, T. M. Klapötke, B. Krumm, and A. Elbeih, "Higher Performance and Safer Handling: Formulation Based on 2,2,2-Trinitroethyl Formate and Nitrocellulose," *Chempluschem*, vol. 83, no. 3, pp. 128–131, 2018.

[20] T. Data, "Doyle's Approximation," vol. 207, pp. 1–2, 1965.

[21] T. Akahira and T. Sunose, "Method of determining activation deterioration constant of electrical insulating materials," *Res. Rep. Chiba Inst. Technol (Sci Technol)*, no. 16, pp. 22–31, 1971.

[22] H. L. Friedman, “Kinetics of Thermal Degradation of Char-Forming Plastics from Thermogravimetry . Application to a Phenolic Plastic,” no. 6, pp. 183–195.

[23] S. Vyazovkin, “Model-free kinetics: Staying free of multiplying entities without necessity,” *J. Therm. Anal. Calorim.*, vol. 83, no. 1, pp. 45–51, 2006.

[24] J. . Coats. A.W., Redfern, “4, 1964,” vol. 201, pp. 68–69, 1964.

[25] J. A. Augis and J. E. Bennett, “Calculation of the Avrami parameters for heterogeneous solid state reactions using a modification of the Kissinger method,” *J. Therm. Anal.*, vol. 13, no. 2, pp. 283–292, 1978.

[26] H. E. Kissinger, “Reaction Kinetics in Differential Thermal Analysis,” *Anal. Chem.*, vol. 29, no. 11, pp. 1702–1706, 1957.

[27] F. Borchardt, J, Daniels, “The application of differential thermal analysis to the study of reaction kinetics,” *Notes Queries*, vol. s6-V, no. 123, pp. 346–347, 1882.

[28] M. A. Hiskey, K. R. Brower, and J. C. Oxley, “Thermal decomposition of nitrate esters,” *J. Phys. Chem.*, vol. 95, no. 10, pp. 3955–3960, 1991.

[29] A. R. Allnatt and P. W. M. Jacobs, “Theory of nucleation in solid state reactions,” *Can. J. Chem.*, vol. 46, no. 2, pp. 111–116, 1968.

[30] J. K. Chen and T. B. Brill, “Thermal decomposition of energetic materials. Part 51. Kinetics of weight loss from nitrate ester polymers at low heating rates,” *Thermochim. Acta*, vol. 181, no. C, pp. 71–77, 1991.

[31] T. B. Brill, P. E. Gongwer, and G. K. Williams, “Thermal decomposition of energetic materials. 66. Kinetic compensation effects in HMX, RDX, and NTO,” *J. Phys. Chem.*, vol. 98, no. 47, pp. 12242–12247, 1994.

[32] C. C. Huang and T. S. Wu, “A simple method for estimating the autoignition temperature of solid energetic materials with a single non-isothermal DSC or DTA curve,” *Thermochim. Acta*, vol. 239, no. C, pp. 105–114, 1994.

3. HIGH PRESSURE BURNING CHARACTERISTICS OF AN ADDITIVELY MANUFACTURED DOUBLE BASE PROPELLANT

3.1 Introduction

In the field of energetic materials, additive manufacturing (AM) can provide more fabrication versatility, logistical relief and strategic military advantages [1]. Exploring novel internal geometries can enhance propellant characteristics such as tailored pressure-time traces that could result in improved performance. AM also allows for a more simplified production chain as additive manufacturing machines can fabricate any desired propellant shape without separate casting and extrusion devices. In addition, some AM methods, vibration assisted printing (VAP) in particular, may allow less solvent inclusion in the propellant formulation, which would minimize toxicity and waste. Calignano et al. provide a recent overview of many different forms of AM and applications [2]. For energetic materials fused filament fabrication (FFF) and direct write (DW) have often been applied. However, FFF uses a meltable filament, which limits applications and may not be safe for thermally sensitive materials.

The traditional method of gun propellant fabrication is die extrusion, where the raw (solvated) propellant material is placed into an extruder and pressed through a shaping die. The extrusion machine uses a piston or extrusion screw to apply significant force to the material. Generally, die extrusion has two main limitations in comparison to additive manufacturing: the geometry of the gun propellant is limited to the geometry of the die, and a modification to the desired propellant geometry often requires machining an entirely new die. Consequently, many '3D' internal geometries (i.e. gyroidal and cubic) simply cannot be manufactured.

Recently, work in energetics additive manufacturing has been done by Toegepast Natuurwetenschappelijk Onderzoek (TNO) and their investigation into using Vat Photopolymerization printing [3]. This process produced working additively manufactured propellants. However, this technique struggled to achieve high solids loadings due to the viscosity of the photocurable mixture. For instance, the digital light process printing was limited to a maximum material viscosity of 20 Pa·s. The team also found that their printed samples were unable to survive test firings and their propellants would shatter and burn incompletely during testing.

TNO has also investigated using a dual material DW printer [4]. This printer used a UV-curable paste and two separate print heads to produce gradated materials. This technique shows remarkable promise to create tailorable propellants, but as of yet, it is unknown if propellant samples have been produced or tested. This printing technique was limited to materials with a viscosity of around 200 Pa·s.

Direct write printing, a technique in which material is continuously extruded using back pressure, has been used by several other groups as a possible solution to print extremely viscous materials [5], [6]. A new form of direct write printing called vibration assisted printing (VAP) was developed at Purdue University. By vibrating the nozzle tip at ultrasonic frequencies, the team was able to print materials with viscosities over 10,000 Pa·s [7].

The objectives of this study are to apply the vibration assisted printing technique to print a viscous gun propellant paste with a minimal amount of solvent content. These printed propellants are then burned in a high-pressure vessel at pressures between 4.3 to 13.8 MPa in order to characterize the burning rate of the additively manufactured gun propellant.

3.2 Methods

3.2.1 Formulation Requirements

In this study, the propellant formulation chosen had to meet the following requirements:

1. All components of the propellant should be chemically compatible.
2. The material should be highly thermally stable and insensitive to extended heating.
3. The material should be compatible with VAP in that its flow rate is highly dependent on ultrasonic vibrations.
4. The dried material should be mechanically sound such that 3D printed samples can survive transportation, handling, and combustion testing.
5. Material should have comparable energetic content to common double base propellants.

3.2.2 Material Selection and Mixing Process

The formulation under investigation is a modified version of an M8 propellant and was chosen due to its high energetic content, its simple manufacturing process and its immediate response to ultrasonic vibrations. The M8 propellant is a double base gun propellant formulation with one of the highest energetic content out of the 'M' series formulations, and is typically used in small arms and artillery applications [8]. Its high energetic content is mainly due to the inclusion of 43% nitroglycerin (NG), in comparison to other 'M' series double base which contain less NG, and triple base propellants which contain a certain amount of nitroguanidine (NQ).

The main modification to the M8 formulation is the replacement of NG with diethylene glycol dinitrate (DEGDN) due to concerns about the thermal instability of NG. DEGDN is an energetic plasticizer that can potentially be used in double base propellant formulations. Specifically, the plasticizer is seen as a replacement to nitroglycerin (NG) in medium to large caliber gun systems because of its improved sensitivity while still maintaining a high energetic content [9], [10]. The formulation is labeled M8D in this study.

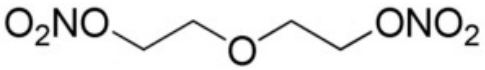

The plasticizer is stabilized in isopropanol until ready for mixing. Prior to mixing, the plasticizer is stored in a dry environment for 120 hours in order to evaporate the isopropanol. The mixing process involves first drying nitrocellulose (NC) for two hours to remove moisture. The NC is then thoroughly dissolved in diethyl ketone (DEK). DEGDN and diethyl phthalate (DEP) are added to the dissolved nitrocellulose and thoroughly mixed for ten minutes. The minor ingredients (potassium nitrate, and ethyl centralite) are then added and mixed for another ten minutes. The paste is allowed to rest in a closed container for one hour prior to printing. Once printing is finished, the samples are dried for 24 hours at 50 C. The formulations of the M8 and M8D propellants are outlined in table 3.1.

Table 3.1. Contents of M8 and M8D formulations.

Ingredient	M8 [7] Wt. %	M8D Wt. %
NC (12%)	52.15	52.15
NG	43.00	–
DEGDN	–	43.00
Diethyl phthalate	3.00	3.00
Potassium Nitrate	1.25	1.25
Ethyl Centralite	0.60	0.60

Note. The M8D formulation uses 33.3% by weight of diethyl ketone (DEK). DEK is used as a solvent due to its low volatility, which allows the propellant mixture to be mixed and extruded through the VAP for long periods of time. After a sample is printed, the DEK is removed from the sample via drying in a vacuum oven.

3.2.3 Vibration-Assisted Printing

A vibration-assisted 3D printer is used throughout this study. One of the major advantages of VAP is its broad material compatibility as VAP has proven capable of printing extremely viscous material. Unlike Fused Deposition Modeling (FDM) methods, its flow actuation mechanism does not rely on heating, and makes it possible to print materials at or near room temperature. As a result, a VAP printer was designed closely following the original design [7]. The M8D paste is loaded into a 10 mL polypropylene (VitaNeedle) air operated syringe with a 0.7 mm needle opening. Minimal pneumatic pressure of 0.30 MPa was applied using an air compressor (California Air Tools). The syringe was connected to the system using a pneumatic syringe driver (McMaster Carr) and pressure regulators allowing for fine control of the back pressure. Ultrasonic vibrations applied at the needle tip and were produced using a function generator (HP 33120A) amplified by a linear amplifier (Piezo System EPA104). Before printing, the desired back pressure, voltage, and frequency were selected, and the syringe was primed for one minute to allow for the flow rate to stabilize. Each formulation went through a series of initial tests to determine its response to VAP. These tests involved finding the paste's minimum extrusion pressure with and without vibrations, and its maximum printing speed with vibrations.

Table 3.2. Slicer settings used to print the M8D propellant paste.

Layer height [mm]	0.3
Print speed [mm/min]	150
Layer width [mm]	0.72

3.2.4 Theoretical Performance Calculations

In order to compare the theoretical performance of the M8D formulation to the M8 formulation, equilibrium calculations were performed using the NASA Chemical Equilibrium Analysis Code (CEA). A total of 161 species were considered in all computations. Both isochoric (constant volume) and isobaric (constant pressure) calculations were performed to assess how the M8D formulation performs in different combustion environments (i.e. a rocket or a gun).

3.2.5 Thermogravimetric and Elemental Analyses

Thermogravimetric (TGA) analysis was performed on M8D samples to assess the thermal stability of the material. M8D samples of 3 mg were used throughout the study. The samples were placed in a DSC-TGA analyzer (TA Instrument Q600 SDT) in an argon environment using a flow rate of 90 mL/min. The samples were contained in alumina pans. The samples were subjected to a 10 minute isothermal at 298 K followed by ramped heating until 573 K. Heating rates of 2, 5, 10 and 20 K/min were used.

Prior to TGA analysis, several nitrocellulose and M8D samples were analyzed for their carbon, hydrogen and nitrogen (CHN) contents using an elemental analyzer. The analysis was performed to ensure that the nitrogen content in the nitrocellulose was relatively constant. The nitrogen content in nitrocellulose strongly influences its solubility, which can cause discrepancies in the mixing. Similarly, the CHN contents in the M8D samples should be relatively consistent to control for energetic content prior to combustion testing.

3.2.6 Density and Porosity Measurements

The density of 3D printed M8D was measured using a gas pycnometer and an envelope density analyzer. The measurements were made at 20 C on slices of a 3D printed strand, each weighing

between 0.35g and 0.4g. Measurements in a gas pycnometer (Accupyc) were performed in a 10cc aluminum cylinder. Helium gas was used due to its low molecular weight and its ability to flow into the external pores of the material, hence measuring a density near the true density of the material. On the other hand, envelope density was measured using an envelope density analyzer (Geopyc). The density is determined by displacement of DryFlo power surrounding the sample. Owing to the relatively large particle size of the solid medium, the envelope density is approximately equal to the non-porous density of the material. Twenty measurements were made with each method.

3.2.7 High Pressure Combustion and Calorimetry

In order the investigate the burning rate of the M8D formulation, small propellant strands measuring 3x3x30mm were cut from a larger 70x30x3mm prism and tested in a closed bomb. The thin material strands were burned in a windowed Crawford bomb (figure 3.1) at pressures of 3.4, 6.9, 10.3, and 13.8 MPa. The bomb was pressurized using compressed Nitrogen to simulate an inert environment. A Nichrome wire was attached to the top of each strand to ignite the strand. The wire was covered in a small amount of nitrocellulose lacquer (Firefox) to affix it to the strand. Finally, the side surfaces of the strand were inhibited using a clear acrylic nail polish. A Phantom v2012 (Vison Research) high speed camera captured the burning of the strand. A 1000 fps frame rate and 4 μs exposure time were used, in addition to strong backlighting. To deduce the burning rate, a MATLAB code was used to track the burning front and a calibration image was used to convert from pixels to mm. The burning rate was obtained from the middle 50% of the strand to ignore discrepancies from the post-ignition and the end-burning regions.

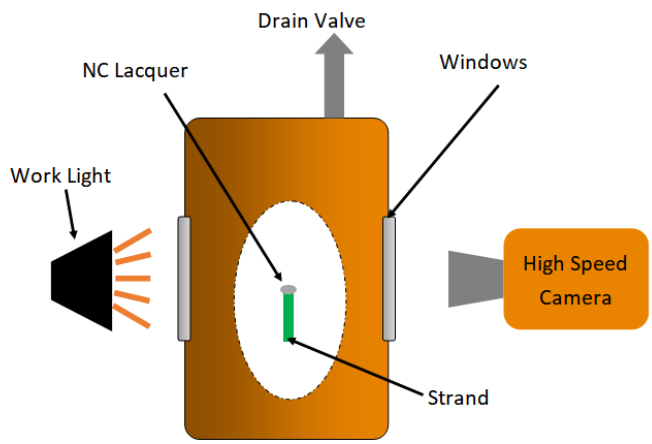

Figure 3.1. Diagram of burning rate test setup using a high pressure windowed bomb.

Furthermore, the energetic content of the M8D propellant was obtained experimentally using bomb calorimetry. Additively manufactured samples of 100 mg were placed in a small-scale bomb calorimeter (Parr), and ignited using a resistive wire. Air was pumped out of the container and excess oxygen was fed inside the vessel at 20 atm in order to ensure complete combustion. The energy content of the burned wire was subtracted from the total heat output to obtain the heat of combustion of the sample. This heat of combustion is taken as the propellant's change in internal energy with respect to standard reference conditions, assuming adiabatic conditions. An experimental heat of formation is then calculated and compared to theoretical values obtained from equilibrium calculations.

3.3 Results and Discussion

3.3.1 Theoretical Performance Considerations

Theoretical equilibrium calculations were performed using NASA CEA to compare both propellant formulations. Table 3.3 summarized the key values for the actual formulation used, while figures 3.2 and 3.3 are used to investigate the effect of different DEGDN and NC contents.

Table 3.3. Summary of theoretical isochoric and isobaric performance comparison between M8 and M8D formulations.

	M8	M8D
Oxygen Balance, [%]	-25.4 to CO_2 5.83 to CO	-44.5 to CO_2 -8.3 to CO
ρ_{th}, $[g/cc]$	1.61	1.51
Isochoric Parameters		
T_v, $[K]$	3539.5	2739.3
f, $[J/g]$	1154.0	1033.9
P_{max}, $[MPa]$	230.8	206.8
Isobaric Parameters		
T_f, $[K]$	2924.5	2201.8
$I_{sp,vac}$, $[sec]$	281.4	257.2
C^*, $[m/s]$	1506.6	1386.8

Note. Isobaric calculations were performed at a loading density $\Delta = 0.2$ g/cc. Rocket calculations were performed at $P = 68$ atm in a fully expanded nozzle.

Figure 3.2 shows several gun propellant performance parameters as a function of DEGDN content, as well as a ternary plot showing the effect of varying ingredient mass fractions on the propellant impetus. The M8 exhibits a nonlinear increase in impetus, pressure and flame temperature, while the M8D formulation performance varies linearly with DEGDN content. A striking difference between the two formulations is that while the M8 propellant performance is higher, it burns at a much hotter temperature, up to 1000 K higher at a 70% plasticizer mass fraction. In addition, the M8D performance is still outstanding. Its impetus is still higher than most single base, double base and triple base gun propellants, while maintaining a lower flame temperature. It can be said that the M8D formulation exhibits characteristics of a high performance small and medium-caliber arms propellant.

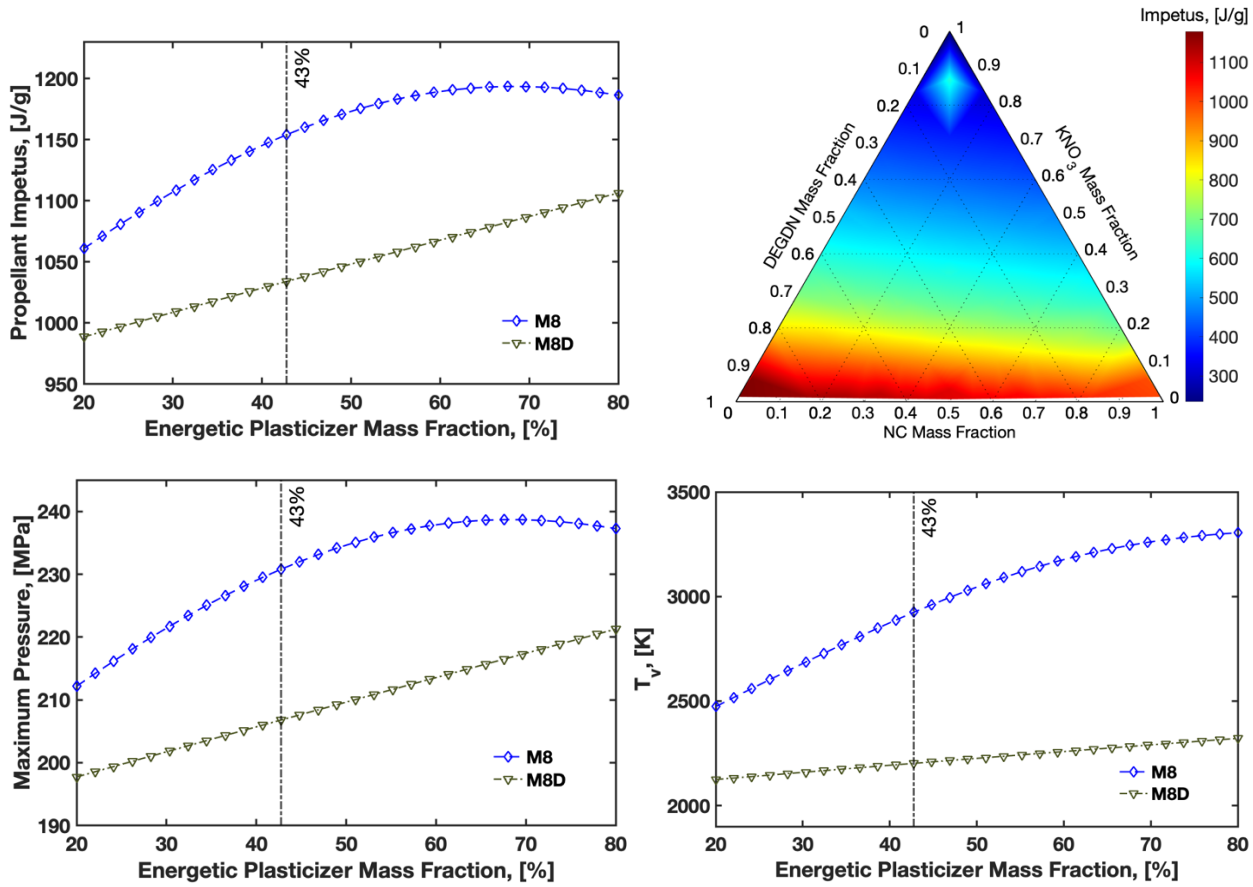

Figure 3.2. Comparison of isochoric performance between M8 and M8D propellants using NASA CEA, performed at a 0.2 g/cc loading density at standard temperature and pressure. Top left: impetus at vacuum as a function of varying DEGDN content. Top right: ternary plot of impetus as a function of DEGDN, NC and KNO3 mass fraction. Bottom: comparison of maximum pressure and closed volume flame temperature as a function of DEGDN content.

Furthermore, figure 3.3 displays rocket performance parameters as a function of DEGDN content, as well as a ternary plot showing the effect of varying ingredient mass fractions on the vacuum specific impulse of the propellant. In general, the M8 formulation exhibits remarkably high specific impulse and C* values throughout, indicating better propulsion and combustion efficiencies, respectively. However, its performance increase comes at the expense of a very high adiabatic flame temperature, which likely discourages using the formulation in a rocket environment. On the other hand, the M8D formulation still retains a high specific impulse and C*, while burning at temperatures 500-1000 K lower than the M8 formulation. These temperatures are closer to those of AP/HTPB/Al propellants used in solid rockets.

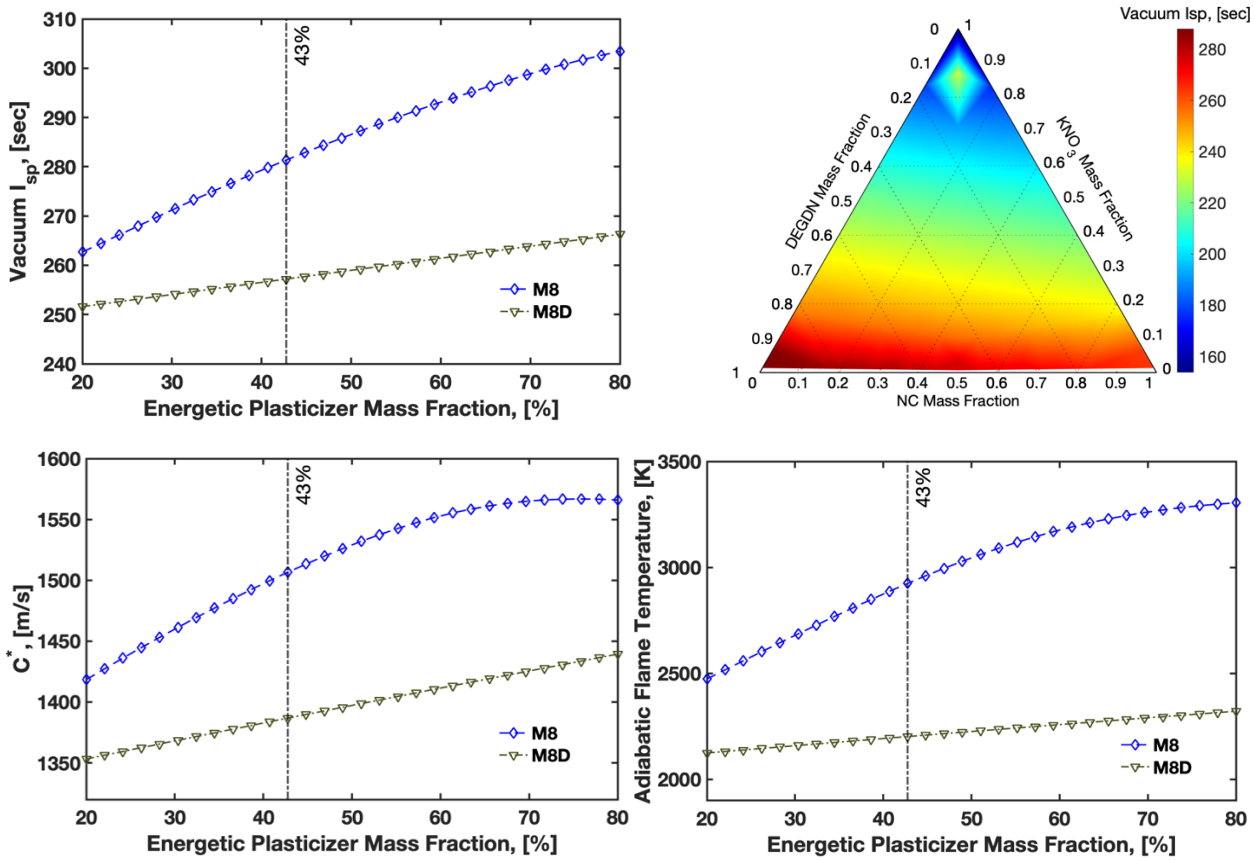

Figure 3.3. Comparison of isobaric performance between M8 and M8D propellants using NASA CEA, performed at 68 atm in a perfectly expanded nozzle. Top left: Isp at vacuum as a function of varying DEGDN content. Top right: ternary plot of Isp as a function of DEGDN, NC and KNO3 mass fraction. Bottom: comparison of C* and adiabatic flame temperature as a function of DEGDN content.

3.3.2 Thermogravimetric and Elemental Results

In order to quantify the thermal stability of the M8D formulation, thermogravimetric analysis (TGA) was performed on M8D samples at various heating rates. Prior to testing, the elemental contents of the nitrocellulose and M8D samples were verified using elemental analysis. The elemental contents of both sets of samples are shown in table 3.4, with special attention paid towards nitrogen content of nitrocellulose. The nitrocellulose used in this study was manufactured to contain 12% nitrogen. The nitrogen content of the nitrocellulose is as expected and shows little variation. Similarly, CHN contents in the M8D samples remain relatively constant across samples.

Table 3.4. Elemental analysis results showing CHN contents of nitrocellulose samples and M8D propellant samples.

Sample	**Mass** $[mg]$	**N** [%]	**C** [%]	**H** [%]
M8D	2.0	12.57	27.93	3.39
	2.2	12.24	27.19	3.40
	2.0	12.46	27.91	3.43
NC	1.7	12.02	26.6	3.01
	1.8	12.31	27.46	3.12
	2.0	11.87	26.8	3.07

In addition, the results of the TGA experiments are shown in figure 3.4 and the relevant temperature and mass loss values are summarized in Table 3.5. Throughout the experiments, the M8D samples did not exhibit any irregular behavior. The M8D decomposition displays two noticeable onsets at lower heating rate values, which progressively merge into one discernable onset at 20 K/min. As the heating rate increases, the total mass loss decreases from 98.3% to 89.6%, which likely indicates that more unburned carbon products are present at higher heating rates.

Table 3.5. Characteristic parameters of M8D and NC decomposition obtained from DSC-TGA analysis

		TGA				DTG		DSC
	$\beta\left[\frac{K}{min}\right]$	T_{oi}	$T_{ot}\,[K]$	$T_{es}\,[K]$	$Mass\ loss$ [%]	$T_p\,[K]$	$T_{oe}\,[K]$	$T_{od}\,[K]$
M8D	2	383.4	441.9	446.6	98.3	446.5	446.63	440.1
	5	399.1	444.0	452.0	96.5	451.9	452.09	439.4
	10	409.1	444.5	458.3	92.8	457.9	458.6	443.5
	20	–	447.8	459.8	89.6	459.0	460.21	444.9
NC	2	–	430.1	466.8	98.3	462.9	469.41	426.8
	5	–	450.3	479.1	96.5	467.2	480.51	436.6
	10	–	455.6	487.8	92.8	484.7	489.91	444.2
	20	–	462.0	495.6	89.6	483.4	500.07	445.7

Note. DTG is the rate of mass loss curve, T_{oi} is the initial onset temperature, T_{ot} is the onset temperature of decomposition, T_{es} is the endset temperature, T_p is the temperature at peak mass loss rate, T_{oe} is the endset temperature of the mass loss rate curve, and T_{od} is the onset temperature of the DSC curve.

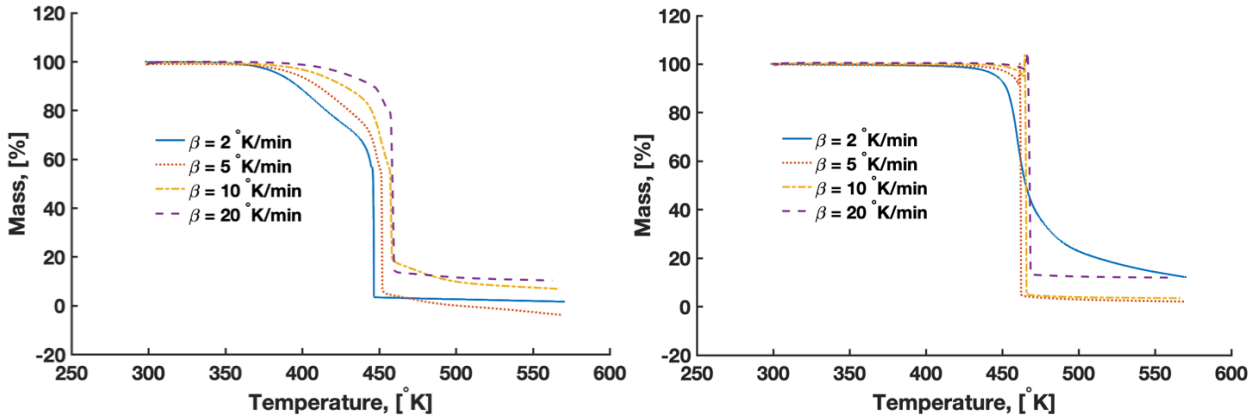

Figure 3.4. Plots of mass remaining as a function of temperature for various heating rates. Left: M8D formulation. Right: nitrocellulose (12% N).

In addition to the sample's mass trace, the material's self-heating effect is demonstrated in figure 3.5. While a constant heating rate is programmed in the DSC TGA experiments, the actual heating rate varies as the temperature approaches the exotherm. Self-heating occurs because the exothermic reactions induce a rapid change in heat output, which changes the sample temperature and may induce some errors in the calculation of kinetic parameters using isoconversional methods. The changes in temperature and heating rate over time are calculated using equations 1 and 2. In this case, the M8D does not exhibit a significant self-heating behavior, where its heating rate varies from 10 K/min to a peak maximum of 11.7 K/min.

$$\delta T = T_{ac}(t) - T_{prog}(t) \tag{1}$$

$$\delta\beta = \beta_{ac}(t) - \beta_{prog} = \frac{dT}{dt}(t) - \beta_{prog} \tag{2}$$

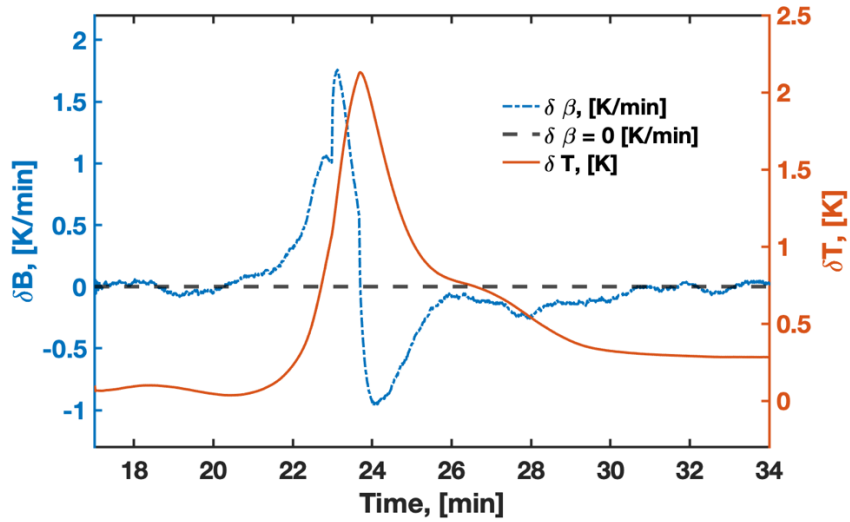

Figure 3.5. Self-heating of the M8D propellant at a programmed heating rate of β = 10 K/min.

The activation energies and pre-factors are then compared using a variety of isoconversional and model-fitting methods [11]–[14]. These kinetic parameters were evaluated at 25 conversion factors, all of which are plotted in figure 3.6. The Afriat (power law) method [12] as well as the Ozawa-Flynn-Wall (OFW) [13] and Kissing-Akahira-Sunose (KAS) [14] methods all output activation energy values that are in excellent agreement. The activation energies using these three methods increase with conversion until $\alpha \cong 0.5$, and then stabilizes at 270 kJ/mol. The values of pre-factors and activation energies are summarized in table 3.6.

Furthermore, the Kissinger and Augis-Bennett methods are contrasted here. The Augis-Bennet (AB) method calculates a much higher activation energy value than does the Kissinger method. This disparity is likely a result of the AB model taking into account the dependence of onset temperature on heating rate, where the difference between the temperature at maximum degradation and the onset temperature is relatively small due to the rapid decomposition of the M8D propellant.

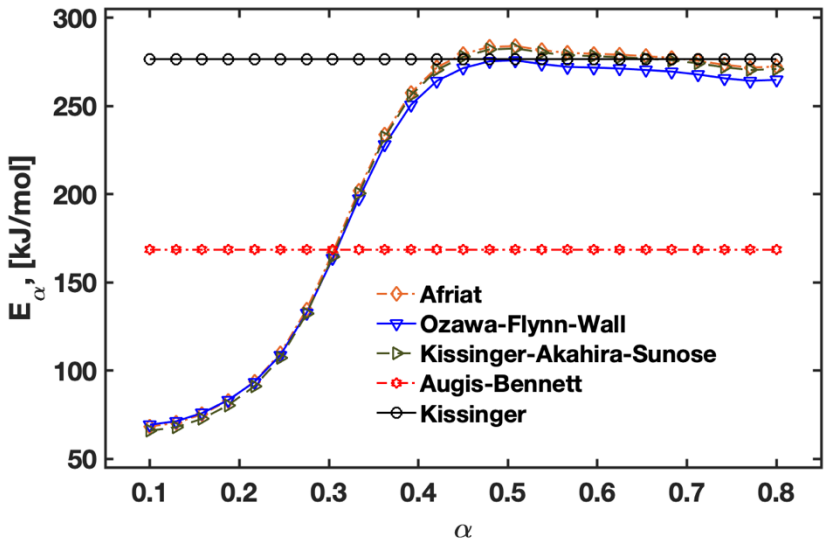

Figure 3.6. Comparison of activation energy values of DEGDN for α = [0.1 – 0.8] using three isoconversional models and two model-fitting methods. The plot displays how the activation energy using Augis-Bennett and Kissinger methods are independent of conversion factor.

In order to reconciliate the disparity between various isoconversional and model-fitting methods, a compensation plot is shown in figure 3.7. The activation energies and pre-factors obtained for different conversions using the Coats-Redfern model are plotted alongside the values obtained using the Afriat model. The lines of best fit are nearly identical, with slopes differing by 0.01 and theirs y-intercepts differ by 0.87. Hence, the activation energy or the pre-factor of the M8D decomposition process, can be obtained using equation 3, where only one kinetic parameter is needed. This compensation equation is nearly identical to that for DEGDN composition [12].

$$\log A\,[s^{-1}] = 0.27E\left[\frac{kJ}{mol}\right] - 6.96 \qquad (3)$$

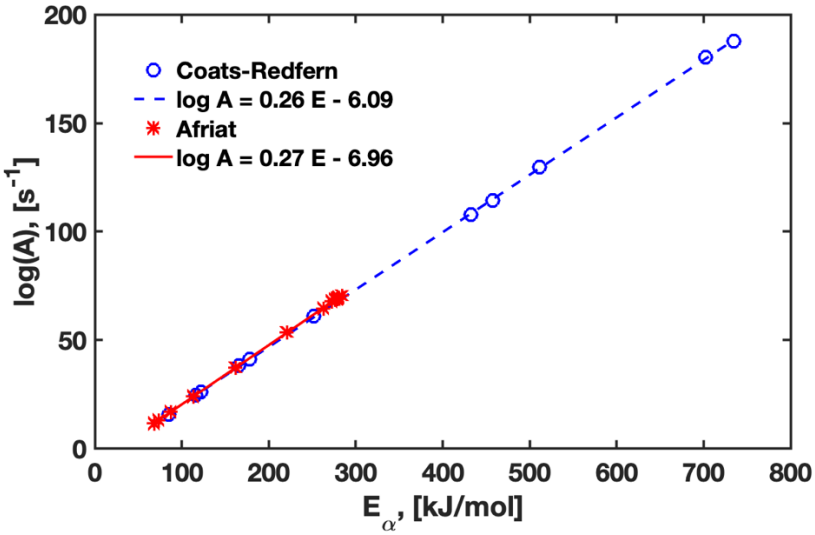

Figure 3.7. Compensation plot of kinetic parameters for M8D propellant decomposition

Table 3.6. Comparison of kinetic parameters between the Afriat and Ozawa-Flynn-Wall models for DEGDN decomposition

	Afriat Model		Ozawa-Flynn-Wall Model	
α	$E_{AFR}, \left[\frac{kJ}{mol}\right]$	$\log A_{AFR}, [s^{-1}]$	$E_{OFW}, \left[\frac{kJ}{mol}\right]$	$\log A_{OFW}, [s^{-1}]$
0.1	68.33	11.57	69.40	12.12
0.2	87.26	16.90	87.33	16.98
0.3	161.82	37.43	158.84	36.47
0.4	262.52	64.68	255.38	62.93
0.5	284.14	70.43	276.05	68.55
0.6	279.53	69.37	271.66	67.53
0.7	276.37	68.68	268.64	66.86
0.8	272.27	67.75	264.74	65.96

The analyses performed above allows to estimate the lifetime of the M8D propellant as well as its autoignition temperature. To estimate lifetime as per equation 4 [15], we define the extent of decay at which the material becomes unusable as α = 0.1. The four isoconversional models used in the analysis output similar lifetime curves (figure 3.8). This analysis is especially important for local heating that the paste may experience either during normal extrusion or in the case of a clog. In order to reach the extent of decay specified in an hour, the sample would have to be heated isothermally at 340 K (estimated using the least conservative model). Similarly, the one-minute lifetime is estimated as 430 K. This sort of heating is highly unlikely to happen in a VAP system, even in the event of a clog.

$$t_\alpha = \frac{g(\alpha)}{Aexp(-E/RT_0)} \tag{4}$$

Lastly, the autoignition temperature can be estimated with reasonable confidence using equation 5. The analysis has been applied to a variety of energetic materials and compared reasonably well to small-scale cookoff experiments [16]. As displayed in figure 3.8, the theoretical autoignition temperature of the M8D propellant at a heating rate of 20 K/min is approximately 424 K using the least conservative method (Friedman's).

$$T_{ign} = \frac{-\frac{E}{R}\sqrt{\left(\frac{E}{R}\right)^2 + 4\left(\frac{E}{R}\right)T}}{2} \tag{5}$$

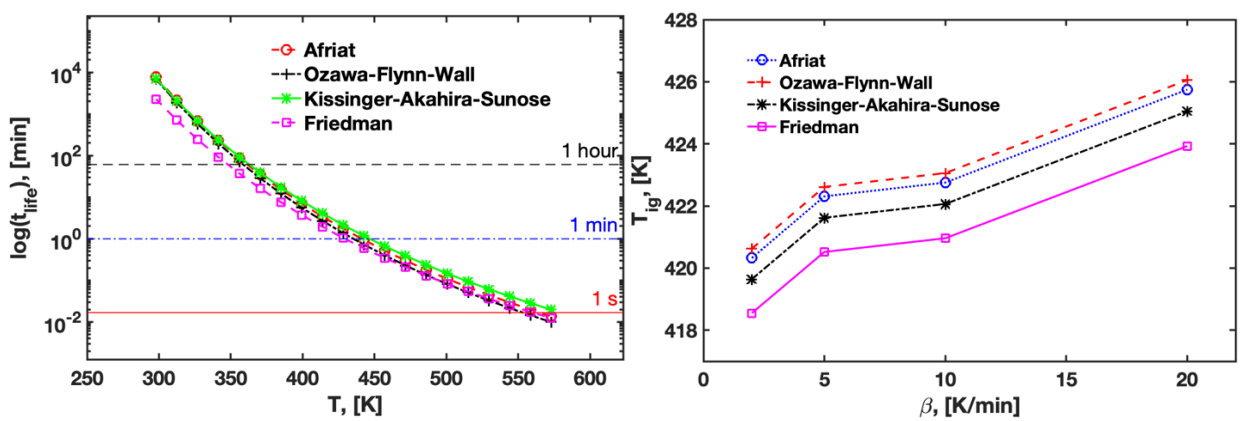

Figure 3.8. Left: comparison of lifetime of the M8D propellant at various elevated isothermal temperatures. Right: comparison of autoignition temperatures for different heating rates.

3.3.3 Print Quality, Density and Porosity

Ensuring the quality of the printed propellant is of utmost importance. Printed propellants should not exhibit any porosity or other internal voids, nor should there be any issues of poor layer adhesion or layer delamination. These printing defects may affect the burning rate and overall burning stability of the propellant. The M8D paste could be printed with low back pressure while the vibrations were active, and the flow can immediately be stopped by turning off ultrasonic vibrations. This tunable flow is highly beneficial for future studies attempting to additively manufacture complex propellant geometries using the M8D formulation. A Hirox MXB-10C fitted with an OL-140 lens was used to inspect the surface and side of each test sample prior to burning. Figure 3.9 shows a microscope image of a printed M8D propellant filament after drying.

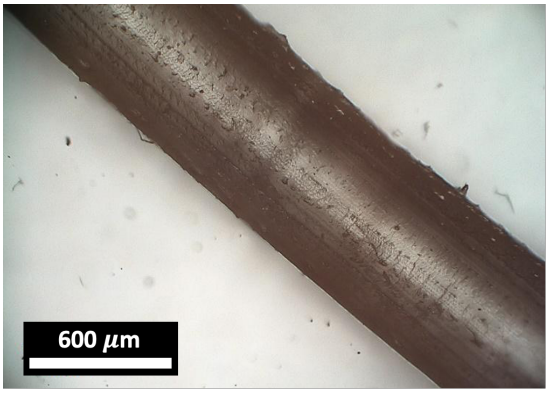

Figure 3.9. Extruded filament of a M8D propellant paste.

A 70mm x 70mm x 70 mm strand was printed successfully. As depicted in figure 3.10, the areas where the material traces intersect are very transparent. However, microscopic inspection released no obvious voids after the material was dried. Figure 3.10 also shows that the layers have not been delaminated. Overall, the VAP system was able to print a sizeable strand sample with straight printing lines with no visible defects.

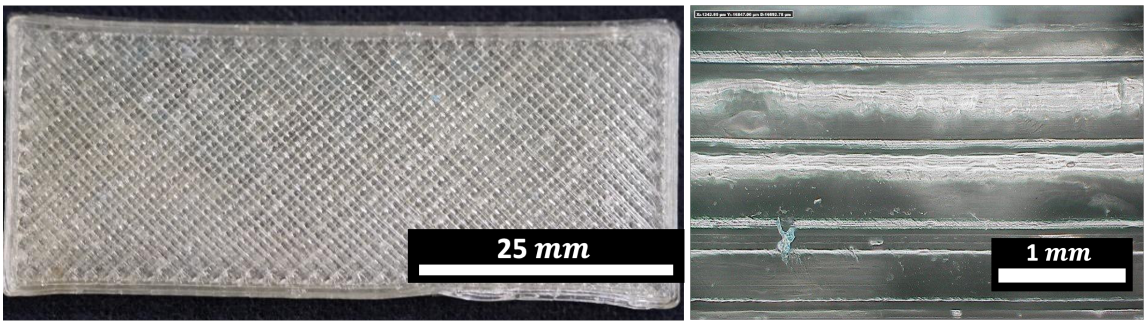

Figure 3.10. Left: Top view of a 70mm x 70mm x 3mm M8D strand after drying. Right: side view of the strand showing no interlayer delamination.

In order to quantify the porosity of the samples, density measurements were performed using a gas pycnometer and an envelope density analyzer (table 3.7). The porosity was calculated as per equation 6. The density using the gas pycnometer is slightly lower than that using the envelope density analyzer. This discrepancy is as expected because the helium gas is able to enter most of the connected pores of the sample, while the envelope density analyzer cannot. The densities only differed by 1.36%, and the porosities were negligible in both methods. The lack of

porosity after drying the solvent is due to visible shrinkage of the material, although volumetric scans have not been performed.

$$\Phi_{\text{th}} = \left(1 - \frac{\rho_{exp}}{\rho_{th}}\right) \cdot 100 \tag{6}$$

Table 3.7. Measurements of 3D printed M8D propellant density and porosity

	Gas Pycnometry	Envelope Density Analysis	Difference [%]
ρ_{ave}, $[g/cc]$	1.486 (0.003)	1.511 (0.004)	1.36
Φ_{th}, [%]	1.65	0.03	

Note. Theoretical density = 1.5115 g/cc, verified using outputs from CHEETAH and NASA CEA. Values in parenthesis are the standard deviation of the measurements.

3.3.4 Burning Rate and Heat of Formation

In order the investigate the burning rate of the M8D formulation, small propellant strands measuring 3x3x30mm were cut from a larger 70x30x3mm prism and tested in a closed bomb. The high-speed video footage was used to analyze the strands as they burned. Combustion stability and burning rate were two factors that could easily be observed from the video. Most of the strand samples were able to survive the Crawford bomb at the tested pressures. During testing, it was found that during ignition many strands would burn slightly unevenly, but as the strand continue burning the burning surface become steady and flat. Figure 3.11 displays this tendency, where the first four frames show an unsteady burning surface, which becomes steady by frame five. This initial instability is mostly attributed to the nitrocellulose lacquer used as an ignitor. In addition, at times the M8D samples tend to emit bright sparks as it burns, possibly due to mixture inhomogeneities such as a high local concentration of potassium nitrate or NC.

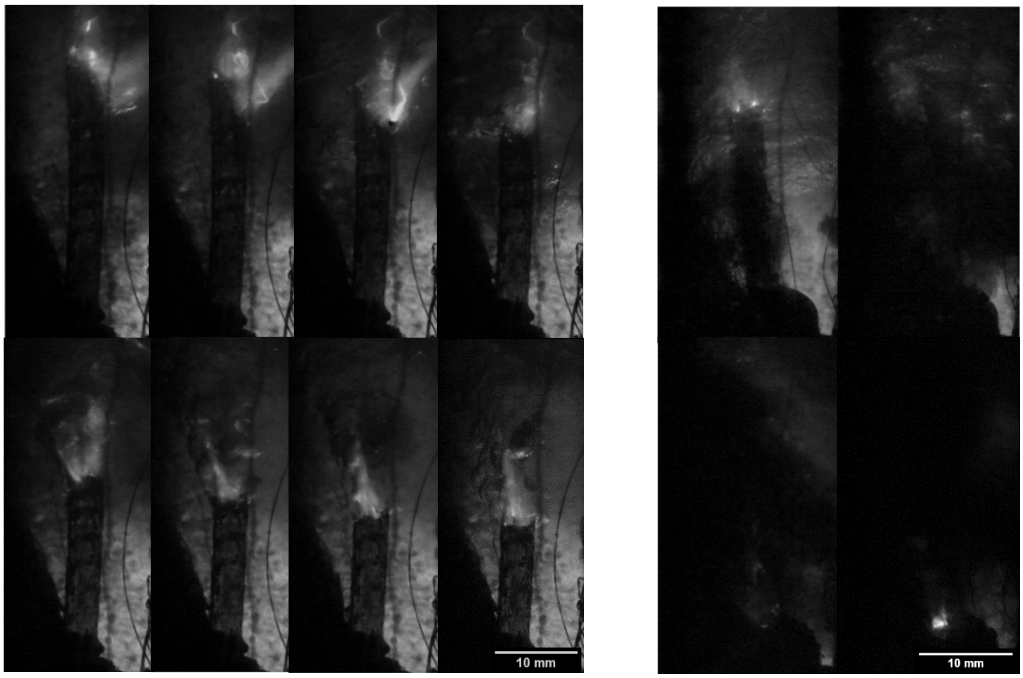

Figure 3.11. M8D strands burning at 6.9 Mpa with 10 ms between frames. Left: example of a satisfactory burn. Right: example of a failed burn.

A couple of strands did not burn adequately. An extreme example can be seen in the above figure. The strand initially is burning normally, however, there is large rapid buildup of smoke in frames 2 and 3. By frame 4 the combustion front comes back into view, and it can be seen that a significant amount of the strand is missing in those interim 30ms.

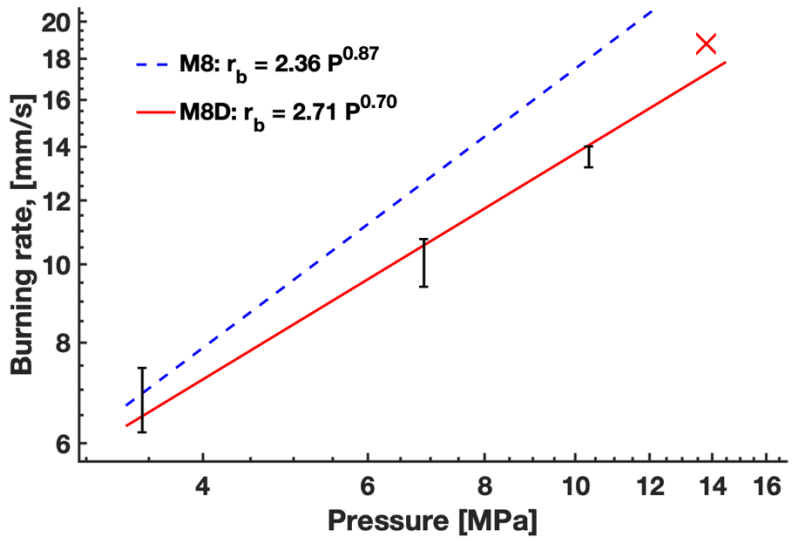

Figure 3.12. Burning rate of M8D propellant as a function of pressure from strand burner tests. $R^2 = 0.96$. The burning rate of the referenced M8 formulation is plotted for comparison.

Burning rate data was fitted using St. Robert's Law (power law) and plotted against the burning rate of the M8 propellant. The referred M8 burning rate law was also obtained using tests from a strand burner. The burning rate exponent of the M8D propellant is slightly lower than that of the M8 propellant. This can likely be attributed to the use of DEGDN in place of NG, as the pressure exponent of NG is near the explosive regime.

Finally, bomb calorimetry was performed with 3D printed samples weighing approximately 100 mg to quantify the energetic content of the propellant. The averaged heat of combustion from the tests was 12506.6 $\pm$ 229 J/g. The standard deviation may be attributed to testing a mixture rather than a pure material, where the effects of non-uniform mixing can cause discrepancies in the heat output. The heat of formation of the M8D samples assuming complete combustion was calculated as -1689.8 J/g. In comparison, the theoretical heat of formation of the M8D propellant from CHEETAH calculations was -2435.9 J/g.

3.4 Conclusion

This work serves as an initial investigation into using VAP as an additive manufacturing technique for propellants with high energetic contents and marks the first time an additively manufactured gun propellant burning at high pressure has been visualized. A modified M8 gun propellant

formulation (M8D) was investigated using DEGDN instead of nitroglycerin. Diethyl ketone was used as the solvent in excess of 33.3% by weight in the manufacturing of the paste. Propellant strands were printed using VAP and high pressure combustion tests were performed to estimate the burning rate of the M8D formulation using high speed imaging. It was found that additively manufactured M8D propellant strands successfully survived high pressure strand burning tests. These tests also showed that as the testing pressure increased, small defects in the printed strands could begin to cause burning instability. Although these defects only affected a minority of samples, the printed propellant quality could be enhanced through refining the propellant formulation and by using longer mixing times. The burning results from the Crawford bomb exhibited relatively low burning rate variance across different tests at the same pressures. This work demonstrates that VAP techniques can be used to additively manufacture minimally-solvated propellants and fabricate highly energetic samples with consistent combustion characteristics.

3.5 References

[1] B. Dolman, A. Hart, I. Johnston, and C. Prior, "ADVANCED MUNITIONS : 3D PRINTED FIREPOWER," pp. 1–4, 2000.

[2] F. Calignano *et al.*, "Overview on additive manufacturing technologies," *Proc. IEEE*, vol. 105, no. 4, pp. 593–612, 2017.

[3] M. H. Straathof, C. A. van Driel, J. N. J. van Lingen, B. L. J. Ingenhut, A. T. ten Cate, and H. H. Maalderink, "Development of Propellant Compositions for Vat Photopolymerization Additive Manufacturing," *Propellants, Explos. Pyrotech.*, vol. 45, no. 1, pp. 36–52, 2020.

[4] M. STRAATHOF *et al.*, "Gradient Printing of Energetic Materials–First Results," pp. 62–74, 2019.

[5] A. Shen, C. P. Bailey, A. W. K. Ma, and S. Dardona, "UV-assisted direct write of polymer-bonded magnets," *J. Magn. Magn. Mater.*, vol. 462, pp. 220–225, 2018.

[6] N. V. Muravyev, K. A. Monogarov, U. Schaller, I. V. Fomenkov, and A. N. Pivkina, "Progress in Additive Manufacturing of Energetic Materials: Creating the Reactive Microstructures with High Potential of Applications," *Propellants, Explosives, Pyrotechnics*. Wiley-VCH Verlag, 2019.

[7] I. E. Gunduz, M. S. McClain, P. Cattani, G. T. C. Chiu, J. F. Rhoads, and S. F. Son, "3D printing of extremely viscous materials using ultrasonic vibrations," *Addit. Manuf.*, vol. 22, no. March, pp. 98–103, 2018.

[8] Krier, "Interior Ballistics of Guns.," *AGARD Conference Proceedings*, no. 392. 1986.

[9] D. A. Reese, L. J. Groven, and S. F. Son, "Formulation and characterization of a new nitroglycerin-free double base propellant," *Propellants, Explos. Pyrotech.*, vol. 39, no. 2, pp. 205–210, 2014.

[10] S. Sun, S. Ma, B. Zhao, G. Zhang, and Y. Luo, "A facile way to prolong service life of double base propellant," *Materials (Basel).*, vol. 11, no. 11, 2018.

[11] H. E. Kissinger, "Reaction Kinetics in Differential Thermal Analysis," *Anal. Chem.*, vol. 29, no. 11, pp. 1702–1706, 1957.

[12] A. Afriat and S. Son, "Isoconversional Power Law Method of Obtaining Kinetic Parameters Applied to the Decomposition of Diethylene Glycol Dinitrate," 2021.

[13] T. Ozawa, "A New Method of Analyzing Thermogravimetric Data," *Bull. Chem. Soc. Jpn.*, vol. 38, no. 11, pp. 1881–1886, 1965.

[14] T. Akahira and T. Sunose, "Method of determining activation deterioration constant of electrical insulating materials," *Res. Rep. Chiba Inst. Technol (Sci Technol)*, no. 16, pp. 22–31, 1971.

[15] S. Vyazovkin, A. K. Burnham, J. M. Criado, L. A. Pérez-Maqueda, C. Popescu, and N. Sbirrazzuoli, "ICTAC Kinetics Committee recommendations for performing kinetic computations on thermal analysis data," *Thermochim. Acta*, vol. 520, no. 1–2, pp. 1–19, 2011.

[16] C. C. Huang and T. S. Wu, "A simple method for estimating the autoignition temperature of solid energetic materials with a single non-isothermal DSC or DTA curve," *Thermochim. Acta*, vol. 239, no. C, pp. 105–114, 1994.

CONCLUSION

Additive manufacturing of gun propellants is an emerging and promising field. The work presented in this thesis demonstrates the feasibility of producing gun propellant grains using additive manufacturing methods. The method chosen was vibration-assisted 3D printing as it has shown to extrude extremely viscous pastes with high loading densities. In chapter 1, the technique was compared to an industrial screw-driven 3D printer where it performed much better in all areas (print speed, print resolution, consistency of porosity and flow turning) except at producing acute overhangs due to sagging. In chapter two, DEGDN, a highly energetic plasticizer, was investigated due to its potential to replace nitroglycerin in double base propellants with high nitroglycerin content. The decomposition kinetics of the plasticizer compared favorably to previously published methods. The material's autoignition temperature was estimated to assess the safety of using DEGDN in a modified double base propellant. In chapter three, a modified double base propellant (M8D) containing DEGDN was additively manufactured using VAP. The print quality, density and porosity of the propellant strands were characterized. Afterwards, the strands were burned at high pressures and the burning rate of the propellant was obtained using high speed video imaging. The burning rate equation as a function of the M8D propellant as a function of pressure was obtained by fitting the burning rate data to St. Robert's Law. Overall, this work shows that VAP is capable of printing highly energetic gun propellants with low solvent content, low porosity, with high printing speeds, and which have consistent burning characteristics at high pressures.